



Ultimate in-plane shear behaviour of clay brick masonry elements strengthened with TRM overlays

A. Y. Elghazouli^{1,2} · D. V. Bompa^{1,3} · S. A. Mourad⁴ · A. Elyamani⁵

Received: 4 February 2023 / Accepted: 11 September 2023 / Published online: 23 October 2023
© The Author(s) 2023

Abstract

This paper studies the response of unreinforced masonry (URM) members made of hydraulic lime mortar and fired clay bricks, commonly found in heritage structures, strengthened with textile reinforced mortar (TRM) overlays. The investigation includes URM and TRM-strengthened diagonal compression tests on square panels, and relatively large-scale wall specimens subjected to combined gravity and lateral cyclic loads. Complementary compression, tension, and interface material tests are also carried out. The diagonal panel tests show that the TRM effectiveness depends in a non-proportional manner on the overlays, render thickness, and substrate strength. The enhancement in stiffness, strength, and ultimate shear strain, using one to four mesh layers on each side, is shown to vary in the range of 49–132%, 102–536%, and 300–556% respectively. It is shown that strut crushing typically governs the response of such low-strength URM masonry elements confined by TRM overlays. The cyclic tests on the comparatively larger walls show that the TRM is effective, shifting the response from URM diagonal tension to rocking, and enhancing the stiffness, strength, and ultimate drift capacity by more than 160%, 30%, and 130%, respectively. It is shown that analytical assessment methods for predicting the response of TRM-strengthened and URM members in terms of stiffness, strength and load-deformation can be reliably adapted. The cumulative contribution of the URM and TRM components, in conjunction with a suitable fibre textile strain, is also found to offer an improved prediction of the shear strength compared to codified procedures. The findings enable the evaluation and improvement of analytical models for determining the main inelastic response parameters of TRM-strengthened masonry and provide information for validating future detailed non-linear numerical simulations.

Keywords Masonry elements · Heritage structures · Clay brick · Lime mortar · Textile reinforced mortar · In-plane behaviour · Shear capacity

List of notations

Latin uppercase

A_i	Area
A_f	Area of the textile reinforcement effective in shear
A_n	Cross-sectional area of the member parallel to the bed joint

A_{str}	Strut cross-section
A_{sw}	Area of shear reinforcement
E	Elastic modulus
E_d	Energy dissipation
E_f	Elastic modulus of the textile
E_m	Elastic modulus of masonry
$E_{m,min}$	Minimum value of elastic modulus of masonry
$E_{m,max}$	Maximum value of elastic modulus of masonry
I	Area moment of inertia
G	Shear stiffness
K_0	Initial stiffness
K_{test}	Test stiffness
K_{eff}	Effective stiffness
K_{el}	Elastic stiffness
N	Axial load
P	Load
P_u	Applied load at failure
\emptyset	Diameter
V_f	Shear force associated with flexural failures (Eq. 7)
V_d	Shear strength controlled by diagonal tensile cracking
$V_{d,lim}$	Shear strength controlled by failure of brick units
V_r	Contribution of the mortar overlay to the shear resistance
V_s	Shear force corresponding to shear sliding
$V_{s,lim}$	Limit shear force corresponding to shear sliding
V_{sc}	Strut crushing capacity
V_m	Contribution of the URM to the shear capacity
V_{mt}	Cumulative shear capacity of the URM and textile
V_{mtr}	Cumulative shear capacity of the URM, textile and mortar overlay
V_{peak}	Test peak load capacity
V_{test}	Test shear capacity
V_t	Contribution of TRM/textile to shear capacity
V_{tr}	Cumulative contribution of the textile and mortar overlay to the shear capacity

Latin lowercase

b	Correction factor depending on the shear stress distribution in the panel and its aspect ratio
d	Member depth/width
d'	Effective compression zone depth
f_b	Brick unit compressive strength
f_{bt}	Brick unit tensile strength
$f_{d,d,e}$	Is the design FRP effective debonding strength
f_i	Strength
f_j	Compressive strength of the joint mortar
f_r	Compressive strength of the render mortar
f_t	Diagonal tensile strength
f_{tk}	Characteristic tensile strength of TRM
f_{tb}	Design stress when debonding takes
$f_{t,r}$	Tensile strength of the render mortar

f_m	Estimated masonry compressive strength
f_{mc}	Measured compressive strength on core samples
f_{TRM}	TRM tensile strength
f_v	Shear stress at failure
f_{v0}	Initial shear strength
f_{v0}'	Cohesion of a brick–mortar interfaces of masonry elements
f_y	Yield strength
h	Height
h_0	contraflexure length
h_b	Height of the brick unit
h_w	Wall height
l_b	Length of the brick unit
n	Parameter for the number of perforations
n_f	Number of reinforcement layers
s_f	Strip spacing
t	Thickness
t_{tot}	Total thickness
t_{vf}	Equivalent thickness
t_f	Equivalent thickness of the sheet
t_f	Equivalent thickness of the sheet
$t_{f,eff}$	effective thickness of the sheet
t_r	Water absorption ratio
w_f	Overlay thickness

Greek letters

α	Crack inclination angle
α_1	Experimental parameter
α_2	Experimental parameter α_1 – reduction factor
α_K	Boundary conditions parameter
β	Angle; biaxial-to-uniaxial strength ratio
γ	Shear strain
ε	Strains
ε_1	Axial strain
ε_b	Fracture fibre strain in bond tests
ε_v	Vertical strains
ε_h	Horizontal strains
ε_f	Fibre strain
ε_{fb}	Ultimate strain from bond tests
ε_{tk}	Characteristic tensile strength from coupon tests
ε_{m1}	Masonry axial crushing strain
ε_{m1}	Masonry axial crushing strain
ε_{TRM}	Fracture strain in TRM coupon tests
$\varepsilon_{lim,conv}^{(\alpha)}$	Conventional strain limit
η	Elastic modulus-to-compressive strength ratio; exposure-dependent factor
ϕ	Curvature distribution
φ	Interlocking coefficient
μ	Slope of the Mohr–Coulomb criterion for singular brick–mortar interfaces
μ'	Slope of the Mohr–Coulomb criterion of masonry elements

μ_{Δ}	Ultimate-to-yield drift ratio
ν	Axial load ratio
σ	Vertical stress, unless otherwise stated
σ_0	Vertical stress in the compressed area of the member, unless otherwise stated
σ_{str}	Strut stress capacity
τ_{mtr}	cumulative shear strength
θ	Rotation or strut angle
τ_u	Shear stress at failure
Δ	Drift
Δ_{test}	Test drift
Δ_{peak}	Drift at peak
Δ_u	Ultimate drifts
Δ_{u2}	Second ultimate drift
$\Delta_{u,URM}$	Drift capacity of URM elements
$\Delta_{u,TRM}$	Drift capacity of TRM-strengthened elements
$\Delta_{f,u}$	Flexural drift capacity
$\Delta_{f,u2}$	Second flexural drift capacity
$\Delta_{v,u}$	Shear drift capacity
$\Delta_{s,u}$	Ultimate sliding drift capacity
$\Delta_{s,u2}$	Second sliding drift capacity
$\Delta_{d,u}$	Ultimate diagonal tensile drift capacity
$\Delta_{d,u2}$	Second diagonal tensile drift capacity
Δ_{γ}	Yield drifts

1 Introduction

Heritage unreinforced masonry (URM) structures typically include various deficiencies in terms of structural form and constituent materials which, combined with poor maintenance over time, can result in significant vulnerabilities with respect to lateral resistance (Fortunato et al. 2017; D’Ayala and Speranza 2003). Irregularities and inadequate connections can also lead to out-of-plane instabilities (Messali et al. 2017; Szabó et al. 2023), whilst material heterogeneity, permanent moisture, and environmental degradation, can all affect the in-plane stiffness, strength, and drift capacity of masonry (Bompa and Elghazouli 2021; Elghazouli et al. 2021).

Previous studies showed that URM elements subjected to combined axial and lateral loading can be characterized by three limit state mechanisms: shear sliding, diagonal cracking, and compressive crushing, forming shear-compression envelopes (Bompa and Elghazouli 2022). To prevent shear-governed failure modes, URM walls can either be strengthened by inserting reinforcement within the bed joints or by surface strengthening (Elghazouli et al. 2022a). In the latter, mortar-embedded reinforcing meshes are attached to masonry with mechanical devices. Alternatively, epoxy adhesives can bond laminates to the masonry. Conventional systems use reinforced plaster or wire welded meshes embedded in a mortar overlay (Kadam et al. 2014; Shermi and Dubey 2017). Other recent systems included polymeric meshes (carbon, glass, basalt, polypropylene bands) referred to as textile reinforced mortars (TRM) (Papanicolaou et al. 2011; Ismail and Ingham 2014; Righetti et al. 2016).

TRM-strengthened specimens typically show three stages in their in-plane response: linear-elastic, cracked, and post-peak. In the first stage, the textile contribution is limited due to strain compatibility in the composite and the mortar overlay acts as a stiffness enhancer (Wang et al. 2019). Following the crack initiation and stabilisation stages in the URM, the load is largely resisted by the textile with an overlay stiffness, akin to that of the elastic response of the dry textile (Almeida et al. 2015; Bertolesi et al. 2014). In TRM-strengthened URM, this behaviour can be superseded by debonding at the masonry-to-overlay interface. Either way, the presence of TRM typically enhances the deformation capacity of the otherwise brittle URM (Bertolesi et al. 2020; Koutas and Bournas 2020). TRM contribution to in-plane resistance can be determined by diagonal panel tests or tests on wall elements under lateral loading. Previous studies have shown that panels strengthened with glass TRM could achieve over a four-fold shear strength enhancement compared to URM counterparts (Ismail and Ingham 2014; Righetti et al. 2016; Papanicolaou et al. 2011). Other studies have also shown that low-cost polymeric grids with a lime-based overlay could increase the ultimate deformation by a factor of 2 to 3 (Umair et al. 2015). The overall in-plane shear capacity is however typically limited by diagonal crushing of the URM (CNR 2018).

The response of walls under lateral loading is influenced by the aspect ratio, axial load level, and the strength and interface properties of mortar and bricks (ASCE 2017; Guo et al. 2022a). Low axial stress levels result in rocking or sliding modes, while high axial stress levels cause diagonal tension and toe-crushing (Moon 2004). Glass textile meshes embedded into a lime fibre reinforced mortar were shown to nearly double the in-plane strength of clay brick lime mortar URM walls under cyclic loading (Torres et al. 2021). Tests on clay brick URM walls with basalt textiles inserted into lime mortar overlays were also found to enhance the in-plane stiffness, strength, and ductility (Garcia-Ramonda et al. 2022). An increase from one to two layers of flax TRM on both sides of clay brick URM elements improved the deformability by over 20% but not in proportion to strength (Trochoutsou et al. 2022).

In the above-mentioned tests, the failure of both URM and TRM-strengthened walls was in diagonal tension without TRM debonding. TRM contribution could be limited if global or local debonding occurs. The former typically involves a leaf separation mechanism when the overlay de-bonds from the substrate, whilst the latter is characterised by local de-bonding in areas of stress localisation such as at the wall toes (Gattesco et al. 2015). In such situations, the TRM prevents diagonal tension and triggers rocking/toe-crushing, modifying the in-plane resistance mechanism (Meriggi et al. 2022).

Several previous studies have assessed the response of conventional URM strengthened with TRM under diagonal compression (Almeida et al. 2015; Papanicolaou et al. 2011; Righetti et al. 2016; Umair et al. 2015; Wang et al. 2019). Other studies have focused on small scale clay brick lime mortar masonry elements with polypropylene (Hračov et al. 2016), basalt (Garcia-Ramonda et al. 2022), or flax (Trochoutsou et al. 2022) TRM, or small and medium scale rubble limestone masonry walls with glass (Gattesco et al. 2015) or basalt TRM (Meriggi et al. 2022), and clay brick masonry with high strength bed joint mortar (Torres et al. 2021; Ivorra et al. 2021). Importantly, none of these configurations are representative of the materials dealt with in this investigation, which is part of a wider research project concerned with heritage masonry structures in Historic Old Cairo (Elghazouli et al. 2018). There is also, more generally, a need to propose reliable analytical models for predicting the inelastic in-plane response of such TRM-strengthened masonry elements.

This paper studies the response of TRM-strengthened and non-strengthened URM elements with hydraulic lime mortar and fired clay bricks, representative of some historic structures (Elghazouli et al. 2021). The tests include panels under diagonal compression and relatively large walls subjected to combined gravity and lateral cyclic loads, coupled with complementary compression, tension and interface material tests. The results assess the TRM overlays effect on stiffness, strength, ductility, and energy dissipation, support future validation of detailed nonlinear numerical simulations, and evaluate and improve analytical models for determining the main inelastic response parameters.

2 Experimental programme

The tests described in this paper include various material and member level experiments, as depicted in Fig. 1. Material characterisation tests were undertaken to assess the fundamental mechanical properties of the masonry and its constituents. Member tests were conducted to quantify the stiffness, strength and ductility enhancements provided by the TRM overlays.

2.1 Constituent materials

All specimens incorporated fired clay solid bricks of size $229 \times 110 \times 66$ mm. The manufacturer-reported compressive strength and water absorption were 13.0 MPa and 10.5 wt.% (Egersund Tegl 2019) whilst the measured values from at least three samples were 14.6 ± 1.1 MPa and 10.5 wt.%, respectively. The bricks and mortar used in the tests replicate thirteenth century Old Cairo heritage structures (Elghazouli et al. 2022b). The bed joints used 1:3 binder-to-aggregate ratio lime-based mortars (Secil Argamassas 2019), while the TRM overlays used a 1:3 binder-to-aggregate ratio of equal parts of lime and cement (Bredon Cement Ltd, 2019). The TRM overlay requires higher strength than the joint mortar to increase the composite wall stiffness compared to the URM counterpart. A lime-cement mix in the render provides strength and compatibility with the masonry (Koutas et al. 2014). The specific gravities of lime, cement, and sand were 2.70, 3.10, and 2.65, with a moisture content of 5% for the sand.

The mortar mixing procedure was according to the guidelines set by EN 1015-2 (CEN 1999a) and EN 459-2 (CEN 2021a). The mortar consistency was evaluated using a flow table as per EN 1015-3 (CEN 1999b). The water was adjusted to get a workable mortar with a flow of 190 mm. The binders and sand were mixed for 180 s until a uniform mixture was achieved, followed by the slow addition of water and continued mixing for a minimum of 180 s. After being cast, the samples were covered with plastic sheets, similar to the masonry components, and taken out of the forms after 4 days.

The mixing procedure followed EN 1015-2 (CEN 1999a) and EN 459-2 (CEN 2021a) standards to produce bed joint and overlay mortars from dry ingredients and water. The fresh mortar consistency was evaluated using a flow table and adjusted to have a workable flow of 190 mm EN 1015-3 (CEN 1999b). The constituents were mixed for at least 360 s (the dry mix of sand and binders for 180 s, and a wet mix with water for another 180 s) until a homogeneous mixture was obtained. The samples were covered with plastic and removed from forms after 4 days. These were kept in laboratory conditions and

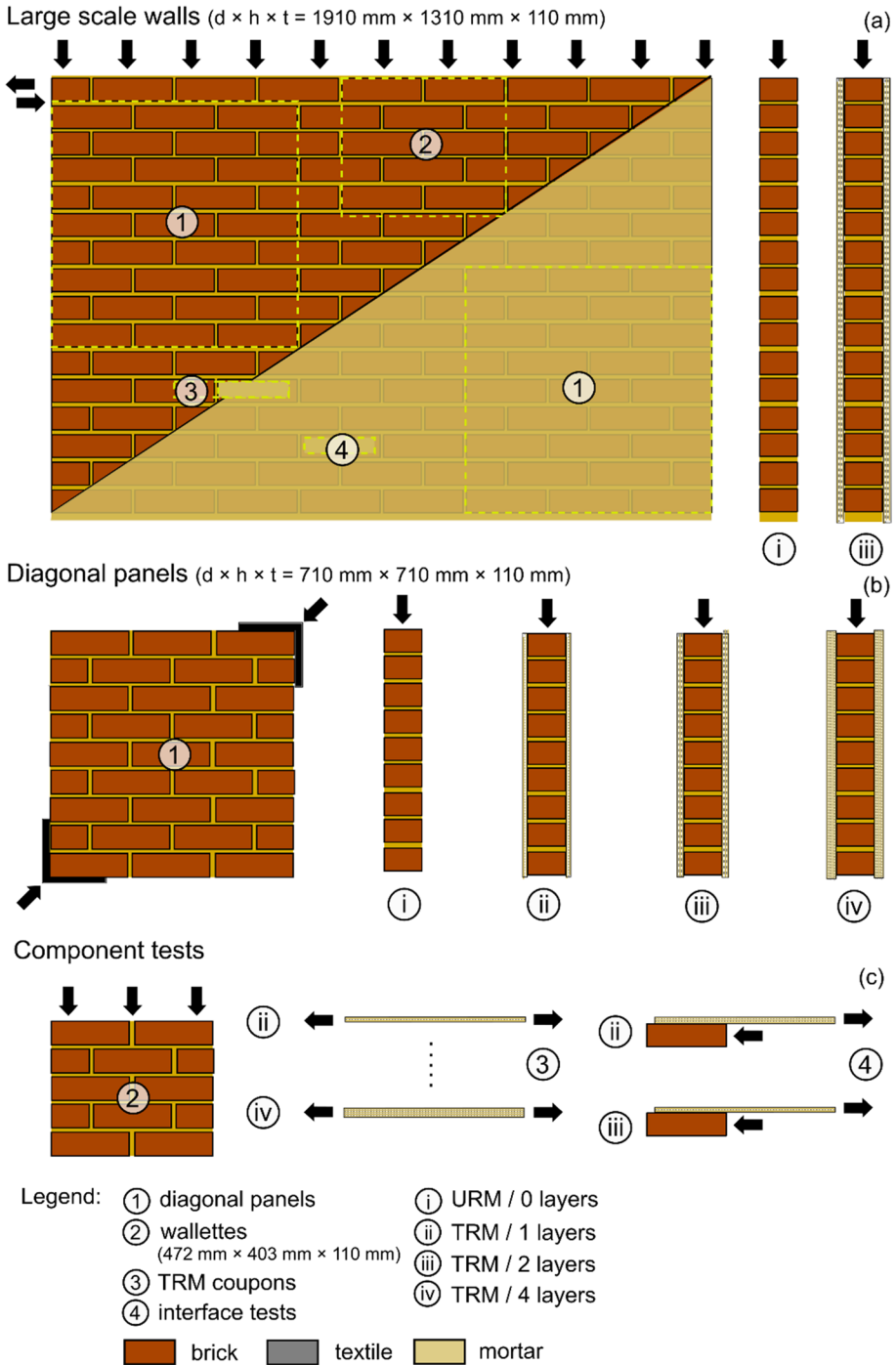


Fig. 1 Specimen details: **a** large wall specimens, **b** diagonal panels, **c** component tests: URM wallettes, TRM coupons, substrate-TRM interface tests (Note: wall sizes exclude TRM thickness)

tested on the same day with the corresponding masonry elements. For each URM wallet or diagonal panel, a minimum of 6 cubes were taken from the joint mortar in addition to 6 cubes for the overlay mortar. For the relatively large-scale walls, 12 samples were taken from the joint mortar of each wall, and 18 cubes from the overlay of the TRM-strengthened wall. At least 6 cubes were also prepared for the TRM coupons and bond tests. In total, over 250 $50 \times 50 \times 50$ mm cubes were therefore tested for strength and had average strengths of $f_j = 1.3\text{--}4.9$ MPa for bed joint mortars and $f_r = 20.4\text{--}32.4$ MPa for render lime-cement mortars. The lower values of f_j were due to higher water content needed to ensure appropriate workability for walls built during the hot and dry summer period (30 ± 5 °C and RH $40 \pm 15\%$) and reflects strength ranges typical of historic masonry.

An alkali and age resistant glass fibre reinforcing mesh was utilized in the TRM, with a 4.0×4.0 mm square mesh size and a weight of 160 g/m^2 (Ceresit 2022). The mesh had a tensile strength of 2075 N/50mm in the warp and 2180 N/50mm in the weft directions. It had an elastic modulus of 72 GPa and an elongation at failure of 3%. The TRM was attached to the masonry substrate using high density polyethylene anchors of 8 mm diameter and 52 mm length, which were provided with a 60 mm diameter disc at the top. This plastic anchor was chosen to avoid possible leaf separation response.

Direct tension tests were conducted on textile mesh strips of 50 mm width in accordance with EN 13934-1 (CEN 2013). The mesh was embedded at the two ends into $75 \times 50 \times 10$ mm (length \times width \times thickness) lime-cement mortar tabs. Aluminium tabs of 1 mm thickness were then glued with a 2-part epoxy to the mortar tabs to ensure adequate local strength and avoid slip from the machine grips. The non-embedded mesh region had a length of 300 mm. The specimen label adopted the format T00-Lx, in which x is the number of layers. The samples were tested in an Instron 250 kN machine at a displacement rate of 1.0 mm/min. A digital image correlation (DIC) system, consisting of two 2.3

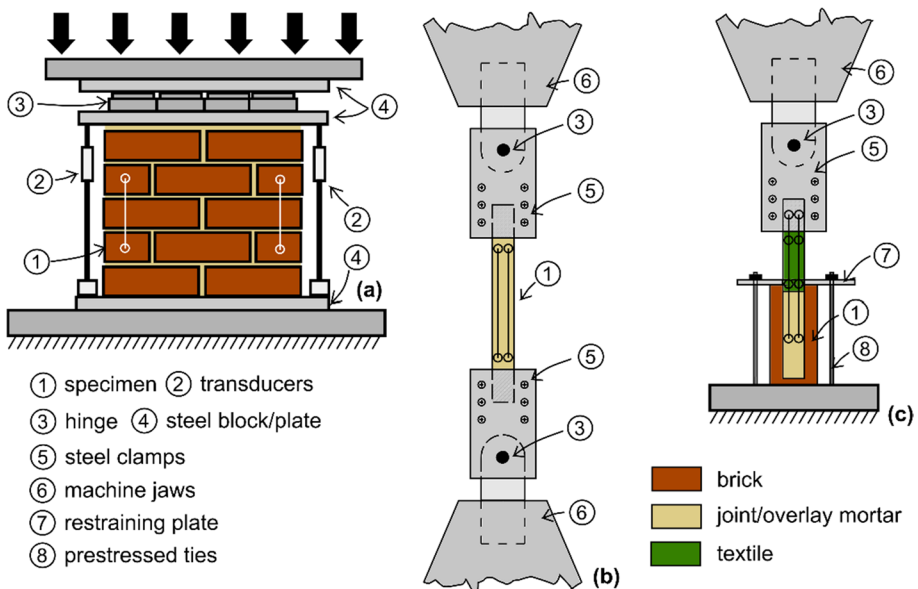


Fig. 2 Component tests: **a** URM wallettes, **b** TRM coupons in tension, **c** TRM coupons in interface shear

Megapixel CMOS cameras (LaVision 2022), was used to record the mesh extension over a gauge length of 135 mm, defined by rectangular targets attached to the textile specimens.

2.2 Component tests

Twelve unreinforced masonry (URM) wall specimens with dimensions of $472 \times 403 \times 110$ mm ($\pm 2.5 \times 5.1 \times 0.8$ mm) were tested to assess the compressive strength of masonry (f_m). The URM wall specimens were constructed following the guidelines outlined in EN 1052-1 (CEN 1999d) with 9 ± 1.5 mm lime mortar joints. The specimens were stored in laboratory conditions and covered with plastic sheets during early curing. They were tested at the same time as the other specimens described in Sect. 2.3. The wall specimens were tested using an Instron 3500 kN machine under compression, as shown in Fig. 2a. The testing setup had a top and bottom steel transfer plate and a hinge attached directly to the machine crosshead. The machine provided load and displacement readings, while two displacement transducers served as a backup measurement system. A DIC system was also used, and the specimen surfaces were painted white and covered with black dots of varying size (0.5–2.0 mm) to create a high-contrast black-white pattern.

A total of 19×50 mm wide and 450 mm long prismatic TRM samples incorporating 1, 2, and 4 layers of textile mesh with lime-cement mortar, with thicknesses of 10, 13 and 20 mm, respectively, were also prepared and tested in direct tension to assess the full deformational response of the TRM render. The thickness and number of layers correspond to the properties of the TRM overlays considered in members. These were in addition to the material tests described before on the plain textile mesh with no mortar. Three samples were prepared for each configuration. The specimen reference adopted the format TRM-Lx, in which x is the number of layers, as indicated in Table 1. For example, TRM-L4 represents a 20 mm thick coupon incorporating 4 layers of mesh. The samples were fabricated in plastic moulds by adding the mortar and textile meshes gradually to obtain the above configurations.

Similar to the mortar cubes, the TRM samples were covered in plastic sheets to ensure the same conditioning and were tested at a similar age achieved by the render at the time of testing the strengthened masonry. The sample ends were provided with 1 mm thick aluminium tabs glued with a 2-part epoxy resin to facilitate end-gripping, as depicted in Fig. 2b. The tests were carried out in a 250 kN Instron machine at a displacement rate of 0.25 mm/min in the elastic regime and 1.0 mm/min in the cracked stage. The same DIC system

Table 1 Mesh, TRM coupons and bond tests results

Sample type	Strength (MPa)	Fracture strain (%)	FM
Mesh	$f_t = 1360 \pm 224$	$\epsilon_t = 2.19 \pm 0.30$	MR
TRM-L1	$f_{TRM} = 2.07 \pm 0.03$	$\epsilon_{TRM} = 1.31 \pm 0.07$	MR
TRM-L2	$f_{TRM} = 3.78 \pm 0.02$	$\epsilon_{TRM} = 1.81 \pm 0.14$	MR
TRM-L4	$f_{TRM} = 5.01 \pm 0.12$	$\epsilon_{TRM} = 1.95 \pm 0.11$	MR
Bond-L1	$f_b = 1193 \pm 326$	$\epsilon_b = 2.39 \pm 0.24$	MR*
Bond-L2	$f_b = 1063 \pm 443$	$\epsilon_b = 3.35 \pm 0.31$	MR

FM failure mode, MR mesh rupture, MR* mesh rupture with some mesh-mortar interface cracking; subscript i = f, TRM, b for textile fibre mesh, textile reinforced mortar, and bond, respectively

mentioned above was used to record the specimen kinematics and assess the surface deformations and strains.

For reference, idealised bond tests between the TRM overlay and masonry substrate were carried out on single-brick single-lap systems to assess the substrate-to-TRM debonding or delamination at the textile-to-mortar interface. Samples with one or two textile layers embedded in a 10 or 13 mm thick lime-cement mortar overlay, respectively, were tested. As in the tension TRM coupons, the width of the mortar component was 50 mm, bonded to the substrate over a length of 200 mm. Prior to placing the first layer of mortar, the surface was brushed, cleaned with compressed air, and painted with a thin film of cement slurry, a procedure also used and described below for the TRM-strengthened masonry elements. The mesh end without mortar was provided with 1 mm thick aluminium tabs glued with a 2-part epoxy to ensure appropriate gripping in the jaws. The samples were tested at a displacement rate of 0.1 mm/min using an Instron 250 kN machine as shown in Fig. 2c. The brick was tied to the machine bed through a purpose-made rig by means of steel plates and threaded rods, to ensure alignment of the mesh axis to that of the machine. As in other tests, a DIC system was used, and the machine recorded the applied displacement and associated load.

2.3 Masonry elements

2.3.1 Diagonal panels

A total of 15 panels (710×710×110 mm) were tested in diagonal compression (Fig. 3a), with 7 un-strengthened and 8 TRM-strengthened panels. The strengthened panels had double-sided lime-cement overlays with 1 to 4 layers of glass fibre mesh. The aim was to determine the influence of mesh thickness, validate resistance expressions for diagonal tension capacity, and evaluate the feasibility of multi-layer mesh overlays. The specimens were labelled in the format 'DX-a', where 'D' stands for diagonal panel, 'X' is the batch (A1 or A2), and 'a' indicates the number of layers (0, 1, 2, or 4). For instance, DA2-0 represents URM panels from Batch A2, and DA2-1 represents TRM-strengthened panels with 1 layer from Batch A2. The two batches differed in joint and overlay mortar strengths, which were proportional and designed for substrate-overlay compatibility (Table 2). Up to 3 specimens were tested for each configuration.

As depicted in Fig. 3b, the panels had 9 ± 1 mm thick lime mortar joints. The specimens were hydrated by water sprinkling before being covered in plastic sheets and tested at 30–35 days. The strengthening process involved applying a primer film, drilling anchor holes, applying a base overlay, placing the textile mesh, inserting anchors, and applying the final coat.

A thin mortar layer of around 3 ± 1.0 was added between each textile layer for multi-layer specimens. Eight symmetrically positioned anchors were used to prevent the overlay-substrate debonding. The overlay thickness varied with the number of mesh layers, ranging from 10 mm for 1 layer to 20 mm for 4 layers. The strengthened specimens, such as that illustrated in Fig. 3c–g, were rendered about 14 days before testing.

The diagonal panel tests were conducted with a 1000 kN Instron machine. Figure 3a shows that the panels were loaded through a hinge and V-shaped supports at the top. A thin timber panel was used between the loading/support plates and the specimen for uniform

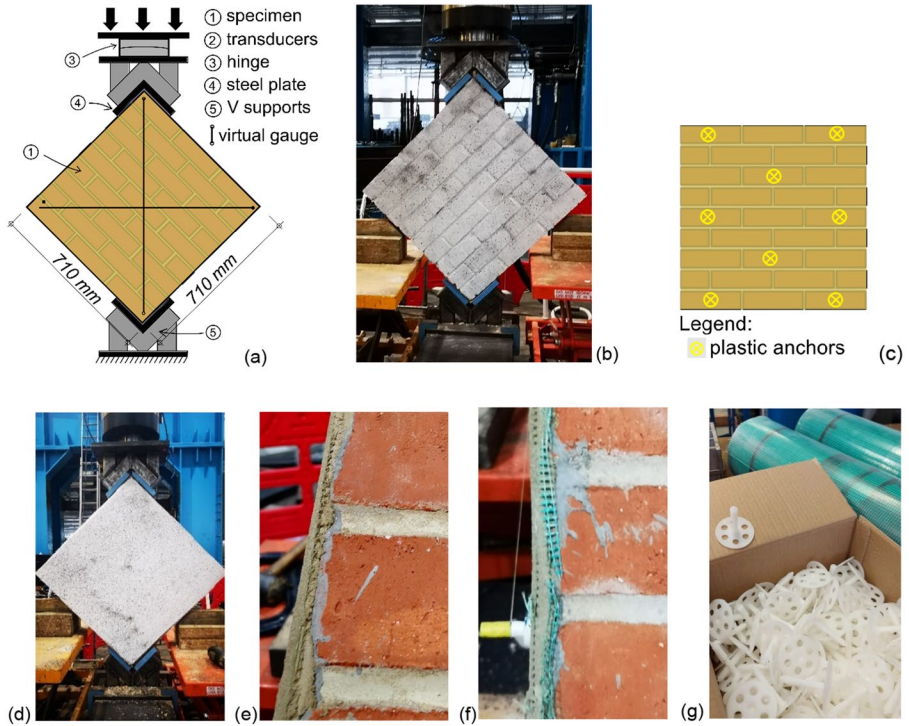


Fig. 3 Diagonal panel tests: **a** schematic representation of testing arrangement, **b** view of a URM specimen, **c** layout of plastic anchors for TRM-strengthened diagonals, **d** image of anchors and mesh, **e** view of a TRM strengthened specimen, **f** close-up of a diagonal panel with two-layer TRM, **g** close-up of a diagonal panel with four-layer TRM

contact. Along with the machine load and displacement readings, two string pots were placed at the back of the panel to measure deformations. The tests were conducted at a displacement rate of 0.5 mm/min, with a DIC system also employed.

Table 2 Main results from diagonal panel tests

Specimen group	P_u (kN)	P_{TRM} (kN)	f_v (MPa)	f_t (MPa)	G (MPa)	f_m (MPa)	f_j (MPa)	f_r (MPa)
DA1-0	26.9±2.4	–	0.24±0.02	0.17±0.02	662±151	3.7±0.1	1.3±0.3	–
DA1-2	120.1±0	93.2	1.09±0	0.77±0	1193±0	3.8±0.1	1.4±0.1	19.6±0.4
DA1-4	144.3±0	117.4	1.31±0	0.92±0	1536±0	3.8±0.1	1.4±0.1	20.8±1.7
DA2-0	74.2±5.1	–	0.67±0.05	0.48±0.03	918±41	5.5±0.1	4.4±0.3	–
DA2-1	149.8±16.4	75.6	1.36±0.15	0.96±0.11	1370±315	5.5±0.1	4.9±0.2	32.7±0.9
DA2-2	158.9±6.2	84.7	1.44±0.06	1.02±0.04	1902±204	6.2±0.2	4.7±0.6	27.6±2.4

2.3.2 Large-scale walls

A pair of walls were also tested under combined gravity and lateral cyclic loads, with focus on directly comparing the behaviour of a TRM-strengthened with a non-strengthened URM counterpart governed by diagonal tension behaviour. As indicated in Fig. 1a, the wall specimens had dimensions of $1910 \times 1310 \times 110$ mm. The specimen size represents a relatively large cut-out from a full-scale wall of a masonry structure such as those investigated in the project. Single-leaf elements were prepared to evaluate the contribution of the TRM overlay, and to avoid specific effects that would appear in full scale walls such as leaf separation. The elements were labelled in the format W1-*a*, where W stands for wall, and *a* indicates the number of layers. For example, WA1-0 indicates a URM wall, whilst WA1-2 indicates a double-sided two-layer TRM-strengthened wall. Both walls were constructed at the same time with DA1 diagonal panels and had similar bed joint mortar strengths. WA1-2 was provided with two mesh layers to appraise and validate capacity expressions for TRM-strengthened walls under cyclic loading as well as to evaluate the practicality of rendering with overlays incorporating more than one mesh layer. Other specimen pairs, for which the non-strengthened URM walls were governed by flexure-type failure, were also tested as reported elsewhere (Elghazouli et al. 2022a, b). However, these are not presented herein since, as expected, it demonstrated that TRM strengthening only had a marginal influence on the performance.

The 16-course high walls (Fig. 4) were constructed using stretcher/running bond and placed on steel plates with a thickness of 25 mm with threaded holes for craning. Both vertical and horizontal mortar bed joints had a thickness of 9 ± 1 mm. The walls were covered in plastic sheets and sprinkled with water for early hydration. The top transfer beam was placed on the URM wall and tied to the bottom support steel plate with prestressing ties 3 days before testing. A cement mortar layer was added for proper bonding and uniform support (Fig. 4a). The assembly was placed on the rig support plate and tied using $6 \times \text{Ø}20$ mm bolts on each side.

The process for the rendered wall was similar to that of the diagonal panels. The steps included: application of cement slurry, drilling of plastic anchor holes, laying of levelling

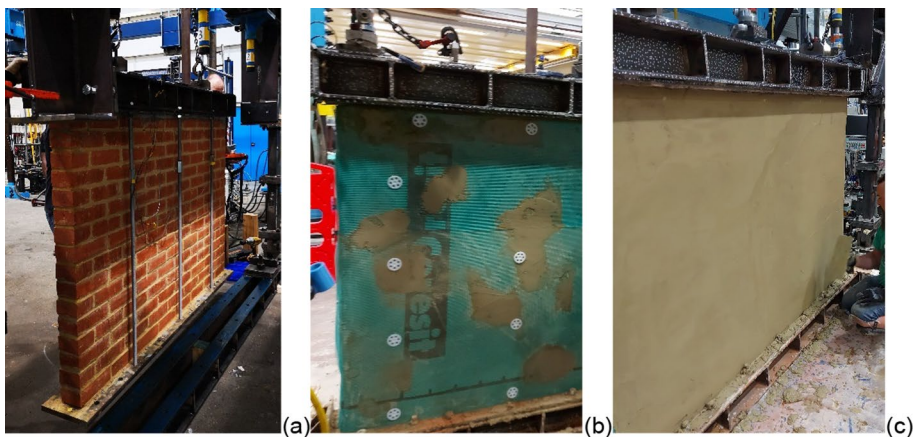


Fig. 4 Large scale specimen preparation: **a** transportation and positioning in the rig, **b** application of the first coat of render, layer of textile mesh and plastic connectors, **c** final rendering

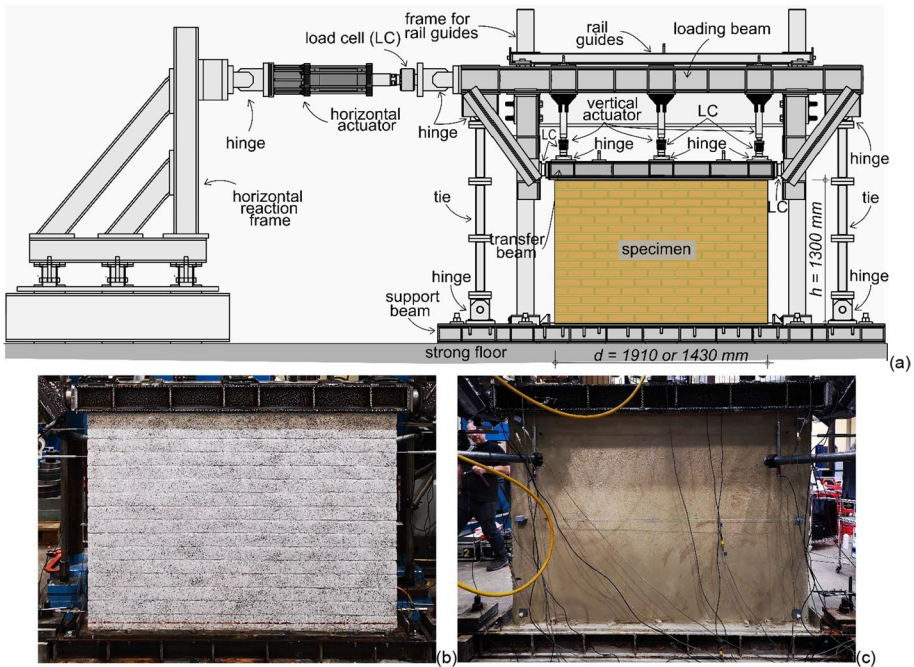


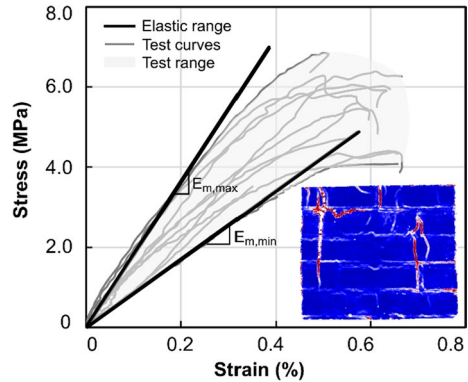
Fig. 5 **a** Schematic representation of the testing arrangement for the large walls; **b** front view of WA1-0, **c** back view of WA1-2

mortar, placement of textile mesh, and final coat application. The overlay was 13mm thick for two layers. The mesh was in 1m wide strips, placed horizontally with 200mm minimum overlap for continuity. A total of 20 transverse plastic connectors were used on each wall face (Fig. 4b). The wall was rendered after being placed in the rig (Fig. 4c).

The test setup aimed to measure the inelastic response under both reverse lateral cyclic displacement and gravity load. The wall was designed as a cantilever masonry structure, where the top transfer beam was allowed to rotate. As shown in Fig. 5, the 25 mm thick support plate was connected to a steel beam through $\text{Ø}20$ bolts and $4 \times \text{Ø}33$ mm pre-stressing ties to prevent sliding or overturning. A steel loading beam at the top of the wall was tied to the support beam through two $80 \times 8\text{ mm}$ ties, and was used to apply gravity load through three 120 kN Enerpac actuators. The lateral cyclic displacement was applied by a 250 kN Instron actuator connected to the reaction frame. Steel elements provided out-of-plane stability to the specimens, following the method described by Elghazouli et al. (2021). The guide rails shown in Fig. 5 were provided with high precision and low friction greased roller ball bearings.

The vertical gravity load and lateral displacements were controlled and monitored using separate units during each test. Loads and displacements were recorded at a frequency of 1 Hz using load cells located at each actuator, two 100 kN load cells between the diagonal transfer struts and the transfer beam, and other measuring devices such as displacement transducers, string pots, inclinometers, and a DIC system. A constant vertical load was first applied, resulting in a vertical stress of $1.08 \pm 0.01\text{ MPa}$. Then, a pre-defined lateral cyclic history was applied, with three cycles at each drift level (%) of 0.025, 0.050, 0.075, 0.10,

Fig. 6 Stress–strain response of compression wallettes and representative crack pattern



0.15, 0.20, 0.25, 0.30, 0.35, 0.40, 0.50, 0.80, 1.0, 1.25, 1.5. This loading procedure was chosen based on existing literature (Petry and Beyer 2015).

3 Test results and observations

3.1 Component tests

Figure 6 shows the stress–strain response of the tested wallettes. The stress (σ) was determined by dividing the load from the load cell (P) by the cross-sectional area. The axial strain ϵ_1 , was obtained from the average of two DIC vertical virtual gauges of 170 mm as per EN 1052-1 (CEN 1999d). The grey curves represent individual tests, whilst the black curves are the minimum and maximum stiffness ranges. It is shown that a linear relationship exists between the compressive strength of the masonry (f_m) and the strength of the mortar joints (f_j) as long as the strength of the brick units remains constant. For relatively low strength mortars with $f_j = 1.3 \pm 0.3$ MPa, $f_m = 3.7 \pm 0.1$ MPa, whilst for relatively high strength mortars with $f_j = 4.7 \pm 0.6$ MPa, $f_m = 6.2 \pm 0.2$ MPa.

The elastic modulus of masonry E_m is typically represented as a function of f_m and a proportionality scalar factor η (i.e. $E_m = \eta f_m$) (CEN 2005a). For $f_m = 3.7 \pm 0.1$ MPa, the elastic modulus was $E_{m,min} = 800 \pm 76$ MPa whilst, for $f_m = 6.2 \pm 0.2$ MPa, $E_{m,max} = 1574 \pm 139$ MPa. These correspond to η values between 216 and 253, which are within typical ranges for lime mortar masonry of 88 to 302 (Costigan et al. 2015; Bompa and Elghazouli 2021), and are significantly lower than those for cement mortar masonry (CEN 2005a). As shown from the σ - ϵ curves in Fig. 6, E_m and f_m are generally proportional. The test crushing strain ϵ_{m1} increases with the decrease in f_m and E_m , which is expected for cohesive-brittle elements. Representative crack patterns obtained from DIC data are shown at the bottom right of Fig. 6. The initial crack was typically located at a vertical joint at the top centre or mid right-hand side of the specimen. In all cases, after crack initiation, the fracture surfaces extended vertically through the adjacent bricks.

The results from tests on the textile mesh, bond specimens and TRM coupons are given in Table 1. These are the ultimate strength (f_i) and corresponding deformation at ultimate (ϵ_i), where the subscript i indicates the sample type ($i=f, TRM, b$ for textile, textile-reinforced mortar and bond, respectively). For example, f_j is the textile strength and ϵ is the textile fracture strain). For the textile, the tensile stress/strength was obtained by dividing

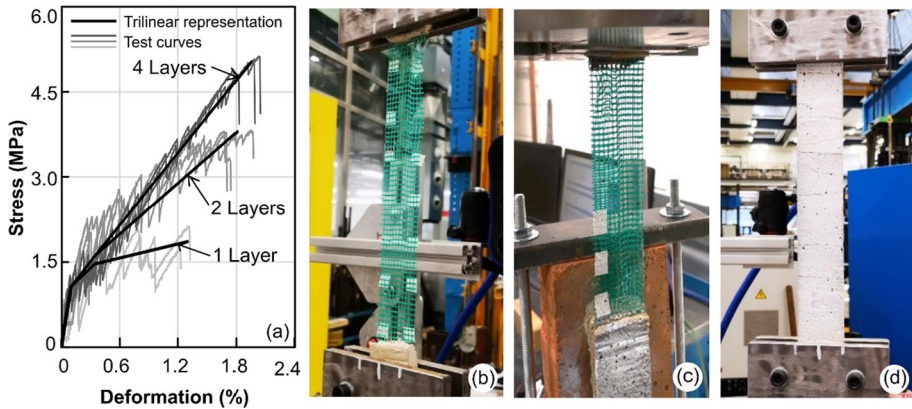


Fig. 7 **a** Stress-deformation for TRM coupon tests, **b** mesh test at failure, **c** interface test at failure, **d** TRM in post-cracking stage

the load by the total sectional area of the longitudinal fibres measured with an optical microscope. For TRM, the same approach was used, but the sectional area of the mortar prism was measured with a digital calliper at 6 cross-sections. For all the tension tests, the deformations were assessed from machine measurements using the distance of 300 mm between grips as the gauge length and validated by DIC measurements from an average of three 135 mm virtual gauges. For the bond tests, the deformation was assessed using a gauge length of 175 mm, which corresponds to the distance between grips and mortar. The joint mortar compressive strength (f_j) from samples tested at the same day as the coupons was 13.3 ± 0.71 MPa.

The textile mesh had a linear-elastic response to rupture with an ultimate strength of 1360 kN and fracture strain of 2.19%, which are lower than the manufacturer values, with the elastic modulus matching the manufacturer data. As indicated in Table 1, the average textile stress at failure from the bond tests exceeded 1000 MPa. On the other hand, the results of the TRM coupons are also summarised in Table 1 and illustrated in Fig. 7a. The figures depict the average stress-deformation response of TRM coupons incorporating 1, 2, and 4 layers of mesh, obtained from 3 test samples in each case. As indicated, the response is largely trilinear with an initial elastic response up to mortar cracking, and a post-cracking response divided into two distinct regions. For specimens with 4 layers, the two post-cracking regimes can be approximated into a single second linear curve to peak strength. This is primarily due to a denser crack spacing. The results in Fig. 7 and the associated Table 1 indicate an enhancement in ultimate strength f_{TRM} and deformation $\epsilon_{u,TRM}$ with the increasing number of textile mesh layers. An increase from 1 to 2 layers, results in an enhancement in f_{TRM} and $\epsilon_{u,TRM}$ by 82.6% and 38.2%, respectively, and by 32.5% and 7.8%, respectively, for an increase from 2 to 4 layers.

Figure 7b–d shows typical views from various tensile tests. Figure 7b shows a mesh sample at failure indicating rupture of the fibres near the top grip. For the bond tests, as shown in Fig. 7c, the deformation was concentrated in the mesh with no sign of deformation or slip at the TRM-substrate interface. On the other hand, Fig. 7d illustrates the typical cracking pattern in a TRM coupon.

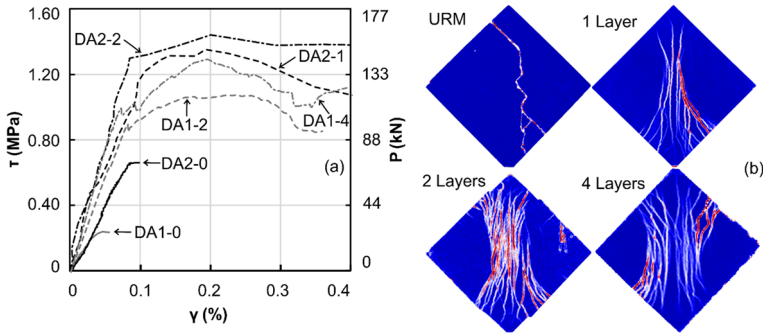


Fig. 8 **a** Shear stress–strain response of diagonal panels, **b** crack patterns for selected panels (URM—DA2-0; 1 Layer—DA2-1, 2 Layers—DA2-2, 4 Layers—DA2-4)

3.2 Diagonal panels

Figure 8a shows the average stress–strain response of the panel specimens, while Fig. 8b depicts the typical crack patterns at failure for selected cases. In these tests, failure is reached when the principal tensile stresses normal to the compression strut created between the two loading shoes, reaches the tensile strength of masonry. At this point, a macro-crack widens and leads to failure (Calderini et al. 2010). This typically arises due to loss of bond at the brick-to-mortar interface (Li et al. 2005; Guo et al. 2022b). In the presence of TRMs, diagonal crack development is delayed and crack opening is restricted (Wang et al. 2019). The impact of TRM on the in-plane stiffness, strength, and ductility depends on the number of textile layers and the reinforcement ratio (D’Anna et al. 2021), as evidenced by a comparison of the shear stress–strain response shown in Fig. 8a, as well as the strength values presented in Table 2, which indicate varying levels of contribution depending on the TRM configuration.

The shear stress and strength were evaluated using ASTM E519-07 principles (ASTM 2007), which assume a pure shear stress in the member (Ferrara et al. 2020). The failure shear stress (τ_u or f_v) was calculated as the ratio of the applied force at failure (P_u) to the cross-sectional area parallel to the bed joints (A_n) (Eq. 1a, 1b) (Bosiljkov et al. 2005). The indirect tensile strength of masonry (f_t) was determined using Eq. (2a, 2b) from the same tests (Hendry 1997; CEN 2021b). The angle of deformation/shear strain (γ), defined by ASTM E519-07, is the sum of the absolute vertical and horizontal strains (Eq. 3) obtained from string pot recordings and validated by DIC measurements. The shear stiffness was assessed in the elastic regime within 10–40% of the peak capacity (Table 2).

$$\tau_u = f_v = \frac{P_u}{\sqrt{2}A_n} \quad \text{where } A_n = ht \tag{1a}$$

$$f_v = \frac{0.707 \cdot P_u}{A_n} \quad \text{where } A_n = \left(\frac{d+h}{2}\right)t \cdot n \tag{1b}$$

$$f_t = \frac{2P_u}{\pi Dt} \tag{2a}$$

$$f_t = \frac{P}{(d+h)t} \quad (2b)$$

$$\gamma = |\epsilon_v| + |\epsilon_h| \quad (3)$$

The URM panels (DA1-0 and DA2-0) showed brittle behaviour, as depicted in Fig. 8, with a linear elastic response followed by limited softening near peak capacity and a sudden strength drop once the critical crack appeared. The TRM-strengthened panels demonstrated superior stiffness, strength, and ductility compared to the URM panels. For panels with lower compressive strength (DA1-0), adding two mesh layers (DA1-2) increased the stiffness and strength by 2.40 and 4.46 times, respectively. With four mesh layers (DA1-4), the factors became 2.88 and 5.36, respectively. For the higher strength masonry panels (DA2-0), one mesh layer (DA2-1) improved the stiffness by 55% and strength by 102%. Two layers of mesh applied on both surfaces of the panels (DA2-2) doubled the strength compared to DA2-0. These enhancements are correlated with a finer and denser crack distribution for panels with thicker overlays and higher number of textile layers. Panels with relatively thin overlays and a single textile layer had fewer cracks which were concentrated near the centre of the panel (Fig. 8b). The masonry-to-TRM interface was intact until the peak, and the governing mode in the TRM was tension. The plastic ties were efficient in preventing overlay-to-substrate separation, which is expected if transverse connectors are provided (Meriggi et al. 2022).

It is shown that the stiffness and strength enhancement varies and is not proportional to the number of mesh layers. Four mesh layers applied on the $f_m = 3.7$ MPa masonry gave a similar member strength as one layer applied to the $f_m = 5.5$ MPa masonry. This is because of different confinement levels provided by the TRM overlays, which influence the crushing capacity of the masonry in the compressed strut. The average ratio of strut stress-to-masonry compressive strength (σ_{str}/f_m) for 1, 2, and 4 mesh layers on each side was 1.17, 1.23, and 1.63, respectively, which is within or marginally above typical biaxial strength ratios for brittle materials. For this assessment, the strut stress (σ_{str}) is the ratio between P_u and the assumed strut cross-section $A_{str} = 212 \times 110$ mm. Clearly, whilst this study considered up to four mesh layers in order to evaluate the feasibility of multi-layer mesh overlays and validate related resistance expressions as noted before, one or two layers would typically represent a common practical choice and mesh layers with higher strength may be considered when required.

In addition to strength enhancement, the ultimate displacement of the strengthened panels, based on a 20% reduction of load in the post-peak regime, was around three times greater than the un-strengthened specimens, indicating an increase in deformation capacity. The TRM strengthens the URM, and after cracking, it bridges the cracks leading to additional ductility.

3.3 Large-scale walls

The test results of large-scale walls under lateral cyclic displacement and axial compression are presented in Fig. 1 and Table 3. The load-drift response is shown in Fig. 9, and the DIC crack patterns obtained at ultimate are displayed in Fig. 10a–d, with the failure patterns shown in Fig. 10e, f.

Table 3 Capacity and deformation characteristics of the large walls

Specimen	WA1-0	WA1-2
N (kN)	227.3	224.2
P_{u+} (kN)	107.1	144.1
P_{u-} (kN)	-114.1	-142.2
P_u (kN)	110.6	143.1
$P_{u,b}$ ($\times P_u$)	0.85	0.95
Δ_y (%)	0.16	0.08
Δ_{peak+} (%)	0.4	0.24
Δ_{peak-} (%)	-0.5	-0.24
Δ_{peak} (%)	0.45	0.24
Δ_{u+} (%)	0.67	1.55
Δ_{u-} (%)	-0.58	-1.38
Δ_u (%)	0.63	1.46
K_{test+} (kN/mm)	44.8	136.6
K_{test-} (kN/mm)	52.5	119.3
K_{test} (kN/mm)	48.7	128
K_0 (kN/mm)	86.3	156.3
K_{eff} (kN/mm)	45.7	123.4
K_{el} (kN/mm)	53.6	125
f_m (MPa)	4.3 ± 0.3	4.3 ± 0.3
f_j (MPa)	2.2 ± 0.5	2.1 ± 0.7
f_r (MPa)	-	20.4 ± 1.3

Note: subscript + and - denote positive and negative cycles, respectively

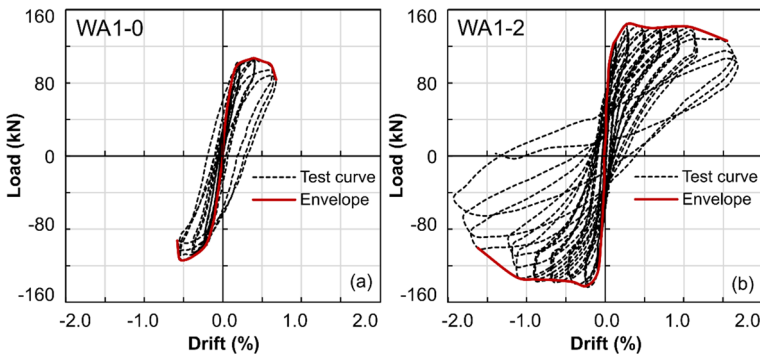


Fig. 9 Lateral load—drift curves for Specimens: **a** WA1-0, **b** WA1-2

3.3.1 Load-deformation response

The URM Specimen WA1-0 had a largely symmetric response in the push and pull directions up to around 90% of the peak lateral capacity. The initial stiffness, corresponding to the slope of the line connecting the positive and negative points of the first loading cycle, was $K_{test} = 48.7$ kN/m. The maximum push (positive) and pull (negative) lateral load capacities were $P_{u+} = 107.1$ kN and $P_{u-} = -114.1$ kN, respectively. As illustrated in Fig. 9a, the

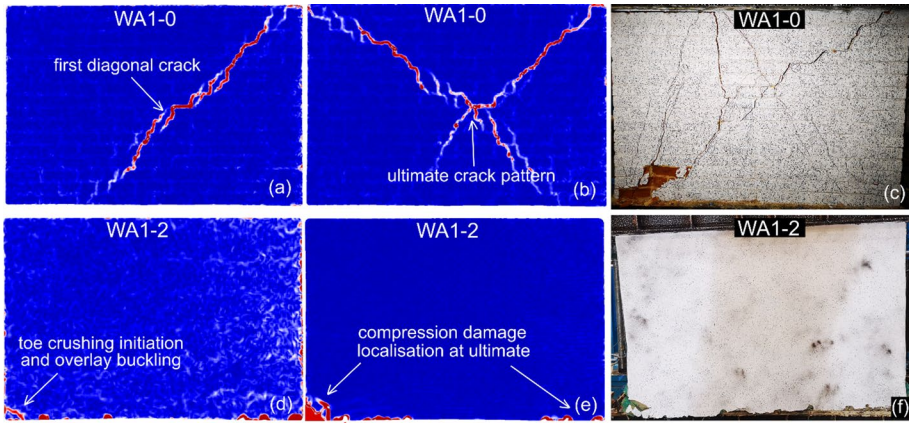


Fig. 10 Crack kinematics: **a** WA1-0 first diagonal crack, **b** WA1-0 ultimate crack pattern, **c** WA1-0 after the test, **d** WA1-2 toe crushing initiation and overlay buckling, **e** WA1-2 damage at ultimate, **f** WA1-2 after the test

corresponding drifts at peak loads were $\Delta_{peak+} = 0.40\%$ and $\Delta_{peak-} = 0.50\%$, respectively. The response was governed by shear as indicated by the failure crack patterns depicted in Fig. 10a, b. The push and pull ultimate drifts associated with a 20% loss of lateral capacity were $\Delta_{u+} = 0.67\%$ and $\Delta_{u-} = 0.58\%$, respectively.

The TRM-strengthened Specimen WA1-2, which was provided with two mesh layers on each side, exhibited a largely symmetric behaviour in terms of elastic stiffness and overall load-drift response. The initial stiffness was $K_{test} = 128 \text{ kN/mm}$ and the lateral capacity was $P_u = 143 \pm 1 \text{ kN}$. By comparing K_{test} of this wall with its non-rendered URM counterpart (WA1-0), it is shown that the cement-lime overlays improved the elastic stiffness by a factor of 2.63. The average Δ at peak was about 46% lower than that of the corresponding URM. As indicated in Fig. 9b, the wall had a largely elastic response up to around 93 kN, similar to that of WA1-0 shown in Fig. 9a.

By comparing the responses of WA1-0 and WA1-2, it is shown that the TRM enhanced the strength by 30.6% compared to the URM wall, due to the suppression of the diagonal crack development by the TRM overlay. The ultimate response of WA1-2

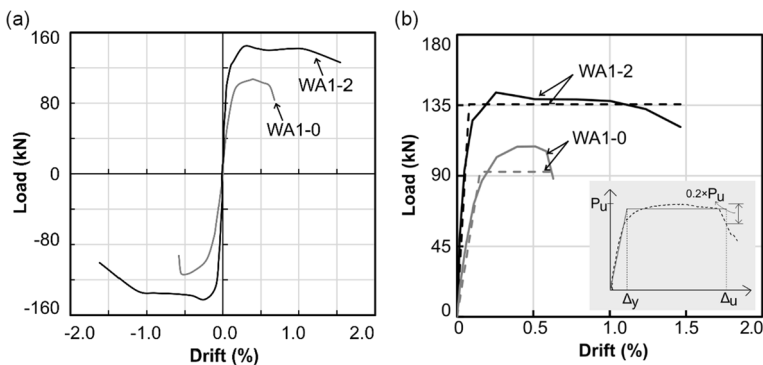


Fig. 11 Load—drift envelopes: **a** full response, **b** average curves

was governed by gradual crushing at the toes during load reversals, combined with gradual buckling of the textile reinforced mortar overlay. The TRM restricted crack development and shifted the failure from diagonal tension to rocking. This is shown in Fig. 10c, d, which indicate diagonal cracking at ultimate for WA1-0 and high concentration of compression strains at the wall toes for WA1-2.

Figure 11a shows the P - Δ curves for lateral load-drift, obtained from first cycle peaks at each drift level. Comparing WA1-0 and WA1-2, the presence of TRM overlay increased both the stiffness K_{test} and capacity P_u , by 162.8% and 29.4%, respectively. The increase in stiffness is due to the contribution of the relatively high-strength mortar overlay, whilst the increase in strength is due to the TRM effectively preventing a brittle diagonal tension failure, which occurs in the URM counterpart.

3.3.2 Drift capacity

In Fig. 11b, the test envelopes (average of positive and negative) and the corresponding bi-linear representations are directly compared for the wall specimens. The bi-linear P - Δ curves were evaluated by considering the energy equivalence between the test and the bilinear idealisation (Tomazevic 1999; Bosiljkov et al. 2005; Salmanpour et al. 2015) and where the linear branch of the latter intersects the test envelope at $0.7 \times P_u$. Apart from Δ_u , which for WA1-2 was greater than that of WA1-0 by a factor of 2.32, ductility can also be considered as the ultimate-to-yield drift ratio $\mu_\Delta = \Delta_u / \Delta_y$. The two drift parameters (i.e. Δ_y and Δ_u) are taken from the bilinear curve (Table 3). Considering this measure, the TRM-strengthened WA1-2 specimen exhibited higher ductility, compared to the URM wall WA1-0, by a factor of 4.65. The TRM increased the stiffness and strength, avoiding brittle failure and significantly improving the ductility of the masonry. The above observations agree with the literature (Torres et al. 2021; Garcia-Ramonda et al. 2022) and with the results from the diagonal panel tests, which showed that the TRM overlay generally increases the ductility of masonry (Fig. 11b). In diagonal-tension governed modes, the TRM reinforcement delays crack initiation, and provides enhancement in strength, ductility, and energy dissipation under lateral loading (Ivorra et al. 2021; Torres et al. 2021). The strengthening technique can change URM in-plane shear failure to more ductile rocking/toe-crushing failure modes.

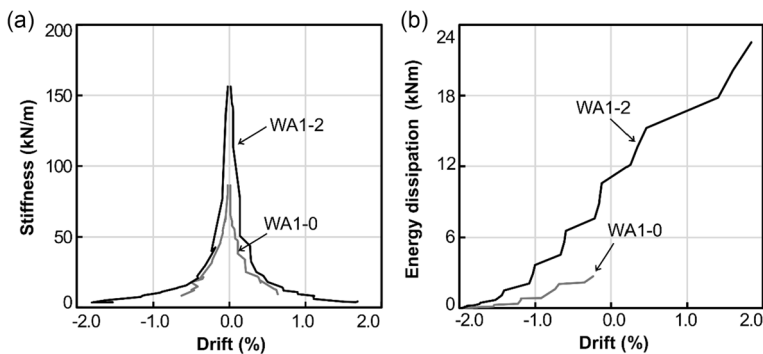


Fig. 12 **a** Stiffness degradation, **b** cumulative energy dissipation

3.3.3 Degradation and energy dissipation

Table 3 gives the main stiffness parameters of the tested walls. The initial test stiffness K_0 , corresponding to the slope of the first loading cycle, provides an indication of the elastic stiffness properties of the tested walls. To assess the stiffness degradation properties of the URM and TRM-strengthened walls, the stiffness was determined for all cycles. Figure 12 depicts the stiffness degradation with respect to K_0 . Positive drift values are associated with unloading stiffness from the foremost positive cycle peak load-drift pair to the foremost negative pair and vice versa.

As shown in Fig. 12, for WA1-0, the reduction in stiffness compared to K_0 was more than 30% at $\Delta=0.04\%$, 50% at $\Delta=0.10\%$, 80% at Δ_{peak} , and 90% at Δ_u . A 20% loss of lateral capacity from peak was associated with a change in drift from $\Delta_{peak}=0.45\%$ to $\Delta_u=0.63\%$ (Table 3). The rendered counterpart (WA1-2) had a higher initial stiffness K_0 . The presence of the TRM overlay increased K_0 by 81%, as shown in Fig. 12. For WA1-2, the reduction in stiffness was more than 30% at $\Delta=0.05\%$, about 50% at $\Delta=0.14\%$, and around 70% at Δ_{peak} .

As discussed before, the response of WA1-2 was more ductile due to a shift in behaviour from diagonal tension in WA1-0, to rocking and toe crushing at ultimate. This is reflected in the longer plateau between the peak ($\Delta_{peak}=0.24\%$) and ultimate ($\Delta_u=1.46\%$) drifts for WA1-2, indicating a lower rate of strength reduction compared to WA1-0. With regard to strength degradation at the same applied drift, as shown in Fig. 9a, b, the hysteresis of WA1-0 and WA1-2 indicate that the strength was largely similar for all three cycles up to around 70% of peak strength. With the gradual increase in inelastic deformations, either due to diagonal cracking for WA1-0 or toe crushing for WA1-2, the strength reduction between the first and second cycle was higher than from the second to third cycle.

The energy dissipation in the wall specimens was evaluated from the hysteretic behaviour in Fig. 9, based on the enclosed areas of cyclic loops at each drift level. Figure 12b depicts the relationship between the energy dissipation E_d and drift Δ for WA1-0 (URM) and WA1-2 (TRM-strengthened). It is shown that at $\Delta=0.5\%$, E_d of WA1-2 was higher than that of WA1-0 by a factor of 3.18 and exceeded two-folds at Δ_u of the URM.

4 Analytical assessments

4.1 Unreinforced masonry (URM)

Strength assessment models typically classify the in-plane response broadly into flexure-governed and shear-governed behaviour. In situations where flexure dominates, a rocking behaviour with little to no diagonal cracking occurs, and failure is often due to toe crushing resulting in a more ductile outcome (Calvi et al. 1996). Shear-governed failures occur through either sliding or diagonal cracking. In case of sliding, the wall slides along a horizontal joint whilst, for diagonal cracking, the response resembles that of the diagonal panels described in Sect. 3.2. High levels of compressive load impose axial restraint which limits the flexural deformations and produce diagonal-tension governed modes, or full crushing of masonry for elements with low compressive strength (Guo et al. 2022a). As noted before, in this study, particular focus is given to URM walls governed by diagonal tension failure, due to the effectiveness of TRM strengthening in these cases.

4.1.1 Shear-governed actions

In design, the governing action is assumed as the minimum of the considered ultimate limit conditions (see Eq. 4). The revised Eurocode 8-3 (EC8-3) (CEN 2021b) differentiates between shear-governed responses (shear sliding V_s and diagonal cracking V_d in Eqs. (5) and (6), respectively) and flexural-controlled response (V_f in Eq. (7)) for the in-plane lateral capacity of URM. Current EC8-1 provisions (CEN 2004) consider only shear sliding (V_s) and flexure (V_f) through Eqs. (5a) and (7), respectively.

Shear sliding can be represented by Mohr–Coulomb criteria (Corinaldesi 2012; Bompa and Elghazouli 2020), as adopted in the current EC8-3 and given in Eq. (5a). This expression requires the actual compression zone depth (d'), which can be obtained analytically, from test measurements, or numerical modelling (Elghazouli et al 2021; Guo et al 2022a). In this study, the reduced depth d' was obtained from analytical assessments. EC8-3 also imposes a limit ($V_{s,lim}$), which differs in the revised EC8-3 (CEN 2021b) (where it is expressed as $0.065f_b$) from the current EC8-3 (CEN 2005b) (where it is given as $0.065f_m$) where f_b and f_m are the brick and masonry compressive strengths, respectively. These equations are valid for $f_m > 2.0$ MPa, hence may not apply for some forms of historic URM.

$$V_m = \min(V_s, V_d, V_f) \tag{4}$$

$$V_s = \left(f_{v0} + 0.4 \frac{N}{d't} \right) d't \leq V_{s,lim} \tag{5a}$$

$$V_{s,lim} = 0.065f_m d't \tag{5b}$$

$$V_{s,lim} = 0.065f_b d't \tag{5c}$$

The diagonal strength V_d of irregular masonry walls is based on the principal stress criterion (right hand side of Eq. (6a) depending on the compression at the bed joints (σ_0), and the diagonal tensile strength f_t (Calderini et al. 2010). This is associated with bed joint stepped sliding, typical for URM with weak mortar. Shear-tensile cracking of bricks can occur when the strengths of the mortar and the bricks are similar (Guo et al. 2022a). The quantity under the square root is multiplied by the element geometry td/b in which d is the masonry wall depth, t is the thickness, and b is a correction factor that considers the shear stress distribution and shape of the panel (h/d , where h and d are the height and depth of the panel respectively, within a range of $1.0 \leq h/d \leq 1.5$).

$$V_d = \frac{t \cdot d}{b} f_t \sqrt{1 + \frac{\sigma_0}{f_t}} \tag{6a}$$

$$f_t = \frac{P}{(d + h)t} \tag{6b}$$

$$V_d = \frac{t \cdot d'}{b} (f'_{v0} + \mu' \sigma) \leq V_{d,lim} \tag{6c}$$

where $f'_{v0} = \frac{f_{v0}}{1 + \mu_0 \varphi}$ and $\mu = \frac{\mu_j}{1 + \mu_j \varphi}$

$$V_{d,\text{lim}} = \frac{t \cdot d}{b} \frac{f_{br}}{2.3} \sqrt{1 + \frac{\sigma_0}{f_{br}}} \quad (6d)$$

The shear strength of regular masonry walls by diagonal cracking uses the Mohr–Coulomb criterion Eq. (6c), relating the shear strength of the panel through parameters f_{v0}' and μ' and the interlocking coefficient φ (CEN 2021b). The parameter φ is the brick height-to-overlapping length ratio. The depth d' in Eq. (6c) is the length associated with the compressed region at the wall end, and the axial stress σ is evaluated for the compressed region ($d' \times t$). Equation 6c is limited by $V_{d,\text{lim}}$ (Eq. (6d)), which adopts the same principal stress criterion, but for failure through bricks. This is captured by the formulation which uses the test tensile strength of bricks (f_{br}), which can be conservatively assumed as $0.1 \times f_b$ (CEN 2021b). The stress σ_0 in Eqs. (6a) and (6d) is the ratio between the axial force N at the panel centre and the full cross-sectional area ($d \times t$).

4.1.2 Flexure-controlled response

In EC8-3 (CEN 2005b; CEN 2021b), the shear capacity for flexural-controlled cases (V_f) (Eq. 7) depends on the wall depth (d), the distance between the section where the flexural capacity is attained and the contraflexure point (h_0), and the axial load ratio ν .

$$V_f = \frac{\nu d^2 t f_m}{2h_0} (1 - 1.15\nu) \quad (7)$$

The axial load ratio ν is the ratio between the axial load N and the compression capacity ($d \times t \times f_m$ of the wall where t is the wall thickness and f_m is the mean compressive strength).

4.2 Contribution of TRM

The in-plane behaviour of a strengthened specimen can be broadly represented by three stages: linear-elastic, cracked, and post-peak. The role of the textile is minimal during the early stages, with the majority of the stiffness improvement arising from the mortar overlay (Wang et al. 2019). The TRM is only activated after masonry cracking, acting as a crack-bridging mechanism which limits crack widths and delays failure (Ismail and Ingham 2014; Türkmen et al. 2020). Debonding, however, can govern the response if the bonded length is insufficient, and the overlay cannot develop its tensile strength (Zampieri et al. 2020). Fibre mesh slip may also occur within the mortar matrix (ACI 2013). Provided that debonding or in-matrix fibre slip do not govern, TRM typically enhances the deformation capacity of URM which is otherwise of largely brittle nature (Bertolesi et al. 2020).

4.2.1 Composites-based models

The current EC8-3 (CEN 2005b) permits the strengthening of URM by means of adequately anchored TRM overlays bonded to either one or both faces of walls. It is suggested that textile meshes should be ductile and preferably inserted in lime-cement mortars. However, there is a lack of information on how to determine the effect of the TRM on the in-plane shear resistance. The draft revision of EC8-3 (CEN 2021b) also allows strengthening by the addition of tensile resisting elements that act in the direction perpendicular to the

bed mortar joints. Reference is made to (Eurocode 6) EC6 (CEN 2005a), which adopts the truss analogy to assess the shear capacity of the strengthened element as the cumulative contribution of masonry and of the strengthening system, but does not provide explicit guidance for TRM. This approach is similar to that for FRP-strengthened reinforced concrete elements which is covered in the current and revised EC8-3 (CEN 2005b; CEN 2021b), and has been used for comparative purposes in TRM-strengthening studies (Thomoglou et al. 2020). Thus, the contribution of surface bonded strengthening systems such as TRM to the in-plane shear capacity of masonry can be added to the URM strength (as shown below in Eq. 8).

Although no specific guidance exists for TRM, Eq. 9a from the draft EC8-3 (CEN 2021b) for the contribution of FRP sheets-strengthened RC members can be adapted to assess the TRM shear capacity. Considering a strut angle $\theta=45^\circ$, that the fibres are parallel to the direction of shear action (as in CNR-DT 215 (CNR 2018) for TRM) i.e. $\beta=90^\circ$, $0.9d \approx d$ wall depth, the strip width $w_f=d$, the sheet spacing $s_f=w_f$ as suggested in EC8-3 and $f_{dd,e}=f_f=E_f \epsilon_{f\beta}$, Eq. (9a) can be rewritten as Eq. (9b). In the code, t_f is the thickness of the sheet, and $f_{dd,e}$ is the design FRP effective debonding strength. Since in TRM-strengthened masonry elements, debonding through splitting of the substrate is unlikely in contrast to FRP-strengthened concrete, the expression for $f_{dd,e}$ in EC6 would not apply (CEN 2005a). In this case, $f_f=E_f \epsilon_{f\beta}$ in which $\epsilon_{f\beta}=0.004$, as used for strengthening of circular sections, would be more suitable.

$$V_{mt} = V_m + V_t \tag{8}$$

$$V_{t,1} = 0.9d(2t_f) \frac{w_f}{s_f} f_{fdd,e} (\cot \theta + \cot \beta) \tag{9a}$$

$$V_{t,1} = 2dt_f E_f \epsilon_{f\beta} = 2 \left(\sum A_f \right) E_f \epsilon_{f\beta} \tag{9b}$$

$$V_{t,2} = 0.9A_{sw} f_y \approx \left(\sum A_i \right) f_i \approx \left(\sum A_f \right) E_f \epsilon_{f\beta} \tag{10}$$

The quantity $d \times t_f$ can be further combined as ΣA_f which is the total area of textile meshes contributing to shear. As noted above, the EC6 (CEN 2005a) model for reinforced masonry walls subjected to horizontal in-plane loads accounts for the cumulative contribution of the masonry and the reinforcement system. The equation is also in the form of $\Sigma A_i f_i$, in which ΣA_i is the horizontal shear reinforcement over the considered part of the wall, and f_i is the material strength, in that case the yield strength of steel rebars (Eq. 10). Based on EC6 (CEN 2005a), the cumulative shear capacity of a masonry wall and the reinforcement system is limited to 2.0 MPa. By using strengthening system-specific quantities, EC6 (CEN 2005a) and EC8-3 (CEN 2005b) expressions are virtually identical.

4.2.2 TRM-specific expressions

Specific expressions to evaluate the influence of TRM on the in-plane shear strength of URM walls are proposed in various design guides. The Italian code CNR-DT 215 (CNR 2018) considers this through Eq. (11a), as the product of a factor accounting for the fibre tensile strength reduction due to shear action ($\alpha_f=0.80$ or measured through tests), the sum

of reinforcement layers on both sides of the wall n_f the equivalent thickness of a layer in the direction parallel to the shear force t_{Vf} , the design dimension of the reinforcement measured orthogonally to the shear force h_w but not greater than the wall depth/length (i.e. $h_w \leq d$), the elastic modulus of the dry textile E_f and the design strain of the textile ϵ_f . In this code, ϵ_f is expressed as the product of the exposure-dependent factor η and the conventional strain limit $\epsilon_{lim,conv}^{(\alpha)}$ (Eq. 11b). The latter is determined from bond tests performed on TRM overlays applied to conventional masonry substrates and multiplied by an amplification coefficient $\alpha = 1.5$, with values other than 1.5 considered if supported by experimental evidence.

The in-plane shear capacity given by the URM and TRM overlays is limited by crushing of masonry (i.e. $0.25 \times f_m \times t \times d$, in which f_m is the masonry compressive strength, t is wall thickness, and d is distance between the extreme fibres of the TRM in tension and compressed masonry, with the fibre direction orthogonal to the shear force). This expression is similar to that adopted in EC6 as an upper limit for reinforced masonry beams subjected to shear loading (CEN 2005a). It is worth noting that if strengthening is applied to a single wall side, the shear capacity should be reduced by 30%.

$$V_t = \alpha_i n_f t_{Vf} h_w E_f \epsilon_f \tag{11a}$$

$$\epsilon_f = \eta \epsilon_{lim,conv}^{(\alpha)} = \eta \alpha F_{max,b} / (A_f E_f) \tag{11b}$$

The North American code ACI 549.6 (ACI 2013) considers the TRM contribution in the form given in Eq. (12). The shear-effective mesh reinforcement area per unit width is denoted as A_f with n representing the number of mesh layers. The cracked elastic modulus of the TRM is represented by E_f and d represents the length of the wall in the direction of the applied shear force. The design tensile strain, $\epsilon_f \leq 0.004$, is similar to the approach in EC8-3 (CEN 2005b) for FRP sheets. The cumulative contribution of the URM and TRM to the in-plane shear resistance is limited by toe crushing. As noted above, this follows a similar form to Eq. (7) for flexural capacity according to EC8-3 (CEN 2005b; CEN 2021b). The more recent version of ACI 549.6 (ACI 2020) jointly published with the RILEM TC 250-CSM report (ACI 2020), adopts Eq. (13) to assess the TRM contribution to in-plane shear. In this expression, n is the wall sides strengthened, A_f is the shear-effective mesh reinforcement area per side, E_f as above is the cracked elastic modulus and ϵ_{fd} is the design axial strain which is limited to $\epsilon_{fd} \leq 0.004$, noting that values greater than 0.004 are accepted if supported by experimental evidence. In both recommendations, the in-plane shear capacity either through stair-stepped sliding or diagonal tension, is capped by the toe crushing capacity.

$$V_t = 2nA_f d E_f \epsilon_f \tag{12}$$

$$V_t = nA_f E_f \epsilon_{fd} \tag{13}$$

$$\epsilon_{fd} = \min(\alpha_1 \epsilon_{fb}, \epsilon_{tk} / \alpha_2) \tag{14}$$

Although Eq. (13) is adopted in the same format in the RILEM TC 250-CSM report (ACI 2020), the design axial ϵ_f strain is the minimum of that obtained from bond tests ϵ_{fb} and tension tests on coupons ϵ_{tk} . The parameters, $\alpha_1 = 1.15$ and $\alpha_2 = 1.25$ in Eq. (14) are both obtained from experimental fitting. This approach is similar to that suggested by

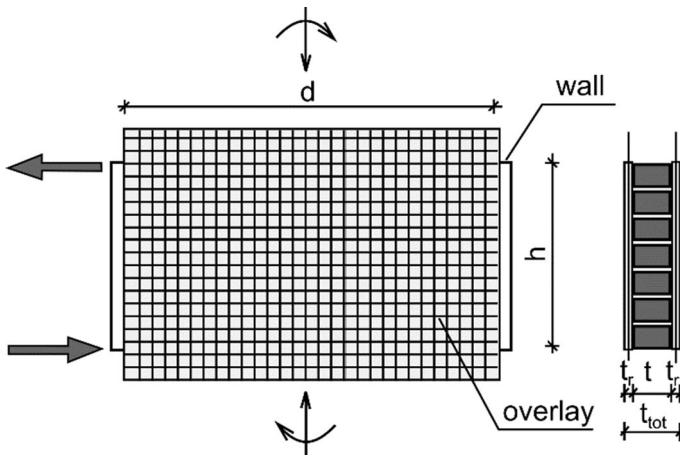


Fig. 13 Schematic representation of the shear action in TRM strengthened walls

Triantafyllou (2016), in which the design strength of the TRM f_f is the minimum between the characteristic tensile strength f_{tk} and the design debonding stress f_{db} . The latter can either be determined from tests or assumed conservatively as $\epsilon_{ib}E_f=0.003E_f$. More recent models account for separate contributions of the mortar and textile to the in-plane shear capacity of the TRM; i.e. $V_{tr}=V_t+V_r$ in which V_t is the contribution of the textile, and V_r is of the overlay (Thomoglou et al. 2020).

4.2.3 Proposed approach

Suggested expressions for the in-plane diagonal tension capacity are given in Eqs. (15). These are based on the cumulative contribution of the URM V_m , of the textile meshes V_t and of the mortar overlay V_r (Eq. 15a). The contribution of the URM is given by Eq. (15b), depending on the masonry type. The resistance V_t is a function of the total area of textile meshes parallel to and in the direction of the shear action as depicted in Fig. 13 (i.e. includes all activated meshes), E_f is the fibre elastic modulus ($E_f=72$ GPa for glass), and ϵ_f is the strain in the mesh at fracture as obtained from tests (see Table 1). In design, a lower value may be considered as noted in the recommendations discussed above. The contribution of the overlay V_r is based on the principal tensile criterion assuming conservatively no influence from the axial stresses (i.e. $\sigma_0=0$). The resistance V_r given by Eq. (15c) is a function of the total overlay thickness t_r , wall depth, the shape factor b and the tensile strength of the render mortar $f_{t,r}$ which can be assumed as 10% of the compressive strength ($f_{t,r}=0.1f_c$), in the absence of specific experimental data.

The ultimate in-plane response of reinforced strengthened masonry may be controlled by crushing (CEN 2005b). As the TRM overlay is compositely connected to the substrate, it provides confinement to the direct strut forming under diagonal compression and enhances the overall strength. Assuming that the strengthened wall is at least in bi-axial confinement, the crushing capacity can be multiplied by a factor β (Eq. 15d). This factor is between 1.15 and 1.20 for cohesive brittle materials, thus a value of $\beta=1.15$ can be conservatively assumed (e.g. Kupfer et al. 1969).

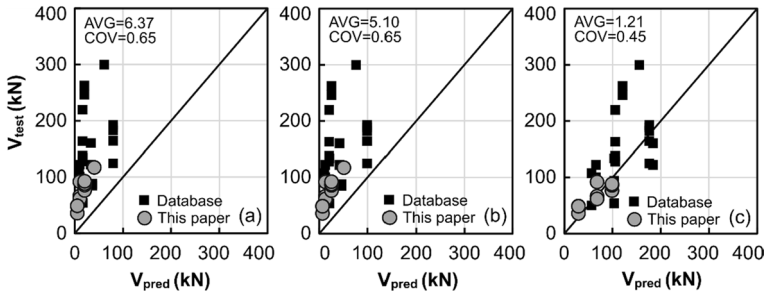


Fig. 14 Predicted vs test TRM strengths using: **a** CNR-DT 215 (CNR 2018), **b** ACI 549.6 (ACI 2020), **c** proposed approach

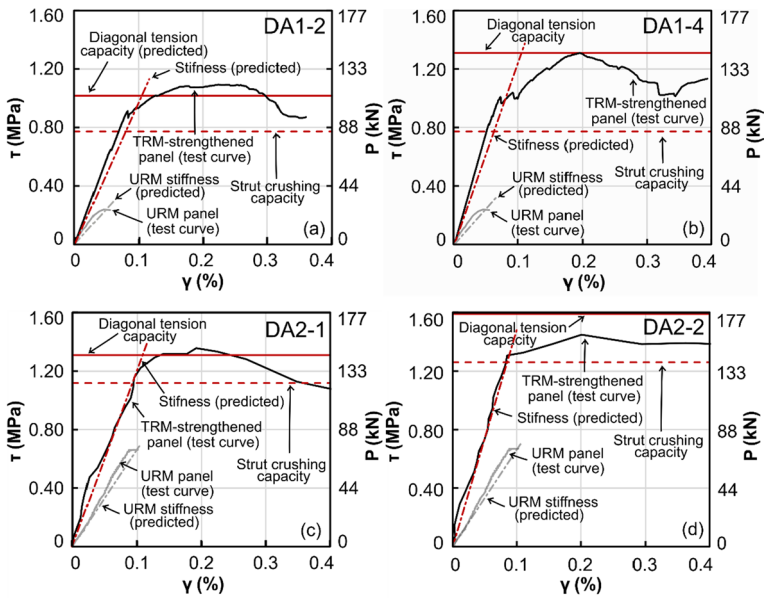


Fig. 15 Comparison between test curves and strength predictions for: **a** DA1-2, **b** DA1-4, **c** DA2-1, **d** DA2-2 (legend: black curves—test data; dashed red line—crushing capacity of masonry under biaxial confinement $\beta \times 0.25 \times t \times d \times f_m$, where $\beta = 1.15$; continuous red line—in-plane shear capacity $V_{mtr} = V_m + V_t + V_r$, where V_m is the URM contribution, V_t is the mesh contribution and V_r is the overlay contribution)

$$V_{mtr} = V_m + V_t + V_r \tag{15a}$$

$$V_t = \left(\sum A_f \right) E_f \epsilon_f \tag{15b}$$

$$V_r = \frac{t_r \cdot d}{b} f_{l,r} \tag{15c}$$

$$V_{sc} = \frac{1}{4} \beta f_m t d \quad (15d)$$

Figure 14 compares the predictions of Eqs. (11–15) and the test results from Sect. 3.2 (grey circles) and from the literature (black squares), whilst Fig. 15 shows a comparison between the test stress–strain curves for the diagonal panel tests and capacity predictions using Eqs. 15. The literature database includes square panel tests which failed in diagonal tension with failure through the TRM overlay. These include clay or tuff masonry, lime or cement overlays incorporating glass carbon or basalt meshes (Prota et al. 2006; Faella et al. 2010; Parisi et al. 2013; Donnini et al. 2021; Marcari et al. 2017).

From Fig. 14 it is observed that existing codes provide an overly conservative estimate of the TRM contribution across all ranges of parameters as indicated by the location of the datapoints and the average (AVG) values shown at the top-left corner of the figure. For consistency, in all code assessments, the design textile strain was considered as $\epsilon_f = 0.004$ as suggested in EC6 (CEN 2005a) for strengthening of circular sections, and ACI 549.6 (2020) for TRM. This indicates that for diagonal tension failures of strengthened walls in which the TRM is fully activated, a higher ultimate design strain can be considered. Figure 14 also shows the predictions of the proposed design-oriented model which includes the contribution of the mortar and the textile separately. Using this approach, the test-to-predicted average is 1.03 and the standard deviation is 0.21 for the tests in this paper, and the corresponding values are 1.21 and 0.45 for the overall database. Note that the ultimate strain used in Eq. 15b is the tensile strain at rupture ϵ_f of the textile either through the tests or from the manufacturer.

The test stress–strain curves of panels described in Sect. 3.2 are shown in black continuous curves in Fig. 15. Stiffness predictions are also shown in the figure with grey and red dash-dot curves for URM and TRM-strengthened panels, respectively. The capacity predictions of Eq. 15a (for the cumulative in-plane diagonal tension resistance) and Eq. 15d (for the crushing strength) are shown in continuous and dashed red lines, respectively. Note that V_m is the test strength of the URM diagonal panel. The shear stiffness G of URM panels was also assessed by multiplying the masonry elastic modulus E_m by 0.5, in which $E_m = \eta f_m'$ with $\eta = 250$ (Sect. 3.1). The multiplication factor of 0.5 is 20% greater than that stipulated in EC6 (CEN 2005a) (i.e. $G = 0.4 \times E$), which is set to provide a lower bound conservative estimate. For the TRM-strengthened panels, a proportionate contribution of the substrate and overlay as a function of their thickness was considered. To assess the elastic properties of the overlay mortar $E_r = \eta f_r$ was used, in which $\eta = 400$ for cement-lime mortars (Bompa and Elghazouli 2021). As illustrated in Fig. 15, the predicted stiffnesses are marginally lower (DA1) or matching (DA2) the tests, indicating that the adopted approach is slightly conservative.

With regard to capacity predictions, the crushing capacity V_{sc} is always lower than the cumulative in-plane shear resistance V_{mtr} . Moreover, V_{sc} is associated with a change in test stiffness, which suggests that the ultimate was controlled by crushing of the direct strut, followed by development of a diagonal crack and by the gradual activation of the TRM. The dashed red line representing the URM strut crushing capacity is close to the proportionality limit (first yield) point for panels with thinner TRMs (DA1-2, DA2-1 and DA2-2), whilst for DA1-4 with the thickest TRM, the difference between the two measures is comparatively greater. This suggests that the biaxial confinement level depends on the TRM thickness and number of mesh layers. The ultimate test capacity is also well captured by Eq. 15 using the fracture fibre strain capacity ϵ_f . The test-to-predicted average is 0.95 and the standard deviation is 20%. These statistical parameters are improved if a lower ϵ_f is

used (e.g. $\epsilon_f=0.004$ as recommended by current guides) which is expected to be the case in design.

4.3 Lateral load-deformation response

4.3.1 Unreinforced masonry

The stiffness of URM walls is usually determined using elastic beam theory and is influenced by the wall geometry, material properties, and boundary conditions (Tomazevic 1999; Benedetti and Steli 2008; Haach et al. 2010). The elastic stiffness (K_{el}), from elastic beam theory and accounting for shear deformation, is evaluated with Eq. (16). The prediction from Eq. (16) was compared with the test stiffness (K_{test}), measured at 10–40% of ultimate capacity, and is shown in Fig. 11.

The elastic stiffness K_{el} is a function of the wall thickness t , length or depth d , height h , elastic bending modulus E , elastic shear modulus G , area moment of inertia $I=t \times d^3/12$, wall cross-section $A_n=d \times t$, and a factor α_K depending on boundary conditions. The parameter α_K is 3.33 for cantilevers, and G is typically 33–40% of E (Magenes et al. 2010; Salmanpour et al. 2013) and can be considered as $G=0.4 \times E$ according to EC6 (CEN 2005a). The effective wall stiffness K_{eff} was also assessed from the bilinear idealisation depicted in Fig. 11b, and directly compared with estimates of Eq. (16). K_{eff} generally varies between 40 and 80% for K_{el} for URM (Bosiljkov et al. 2005). Based on the assessments in this paper, it is shown that the K_{eff}/K_{el} ratio is around 85% for the non-strengthened wall.

$$K_{el} = \frac{1}{\frac{h^3}{\alpha_K EI} + \frac{h}{A_n G}} \tag{16}$$

The lateral load-deformation ($P - \Delta$) response of URM walls can be represented by a piecewise linear relationship that considers strength degradation (CEN 2021b). The idealized relationship has two branches, the first up to 70% of the peak strength, represented by the elastic stiffness K_{el} , and the second at 50–75% of K_{el} . The strength between the yield Δ_y and ultimate Δ_u drifts is assumed constant. The second branch continues to a ‘second’ ultimate drift Δ_{u2} , which is 4/3 of Δ_u , with the slope depending on the failure mechanism (flexure, sliding, or diagonal tension). The drift parameters Δ_u and Δ_{u2} are associated with the ‘Significant Damage’ and ‘Near Collapse’ limit states, respectively.

Based on EC8-3 (CEN 2005b), the ultimate drift capacity in flexure-controlled cases is $\Delta_{f,u}=0.008h_0/d$, and is suggested as $\Delta_{v,u}=0.40\%$ for shear-governed situations. In EC8-3 (CEN,2021b), $\Delta_{f,u}=0.01(1-\nu)$, where ν is the axial load ratio, and the second drift $\Delta_{f,u2}=1.33\Delta_{u,f}$ corresponds to 10% reduction in shear force (for regular masonry, increasing to 20% for irregular masonry) in the post-peak range. For the revised (2nd generation) version (CEN 2021b), a value of $\Delta_{s,u}=0.8\%$ is proposed; however, if the masonry unit strength ($V_{s,units}$) limits the shear sliding, a value of $\Delta_{s,u}=0.5\%$ is recommended, with $\Delta_{s,u2}=1.33\Delta_{s,u}$. Equation (5a) is used to evaluate the residual shear strength at $\Delta_{s,u2}$. If $V_{s,units}$ governs the shear sliding, the residual shear strength is assumed as half the sliding strength without the contribution of f_{v0} . For diagonal failure, $\Delta_{d,u}$ is considered as 0.6% for regular (stair-stepped joints) masonry, and as 0.5% for irregular masonry, with $\Delta_{d,u2}=1.33\Delta_{d,u}$. For regular masonry, the residual shear force at $\Delta_{d,u2}$ is assumed as 50% of the shear resistance, reducing to 30% for irregular masonry.

4.3.2 Strengthened masonry

Provided that full composite action between the overlay and the substrate can be assumed in the elastic regime of TRM-strengthened walls, the stiffness K_{el} can be evaluated from the cumulative contribution of the components, namely the URM, considered above, and the TRM overlay. For the strengthened wall specimen (WA1-2), the ratio K_{eff}/K_{el} is 0.98, and the contribution of the masonry to K_{el} is 51%, whilst that of the overlay is 49%.

According to EC8-1-2 (CEN 2021c), the drift capacity of reinforced masonry members may be assumed as 1.5 times the URM, unless demonstrated otherwise by tests whilst, according to EC8-3 (CEN 2021b), the deformation capacity is 1.33 the URM, provided that detailing is compatible with EC6 (CEN 2005a) recommendations. ASCE 41-17 (ASCE 2017) provides a wide range of drift limits for reinforced masonry walls under in-plane actions depending on the aspect ratio, reinforcement ratio, axial load, and a residual strength ratio. The second drift limit in EC8-3, Δ_{d2} , and associated strength, can be correlated with the drift and corresponding strength obtained by applying the residual strength ratio in ASCE 41-17 (ASCE 2017). These drifts vary within 0.2%–2.6% as a function of the wall aspect ratio, reinforcement ratios, and axial load. For shear-governed walls with axial load ratios above 0.15, the element is considered to have a brittle response with no ductility, as a ‘force-controlled’ mechanism.

As shown above, deformation limits exist in seismic assessment and retrofitting codes [i.e. EC8-3 (CEN 2021b) and ASCE41-17 (ASCE 2017)]. However, these are for masonry reinforced by steel rebars, and cannot be applied directly to URM strengthened with TRM overlays. Although TRM-specific recommendations acknowledge the enhancement in deformation capacity, they do not provide expressions to quantify the deformability of TRM-strengthened URM (CNR 2018; ACI, 2020). A direct comparison between the test drift capacity of masonry walls strengthened with basalt TRM, and those stipulated in the current EC8-3 (CEN 2021b) and the Italian standard CNR-DT 215 (CNR 2018) for URM, indicated that both standards underestimate greatly the deformation capacity both at SD and NC (Garcia-Ramonda et al. 2022). This points to the need for specific limits that can be used for TRM-strengthened masonry.

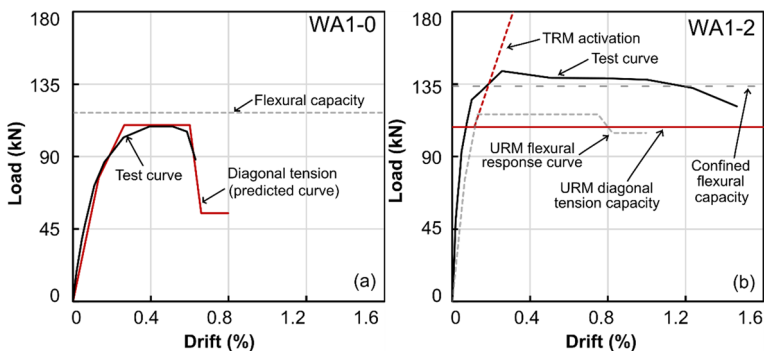


Fig. 16 Comparison between average test envelopes and predictions of code expressions for: **a** WA1-0, **b** WA1-2 (Legend: black curves—test envelopes, continuous red curves—diagonal tension capacity, dashed red curve—TRM activation, dashed grey curves—capacity, dash-dot grey curves flexural capacity multiplied by $\beta=1.15$ accounting for the confinement produced by the TRM overlay)

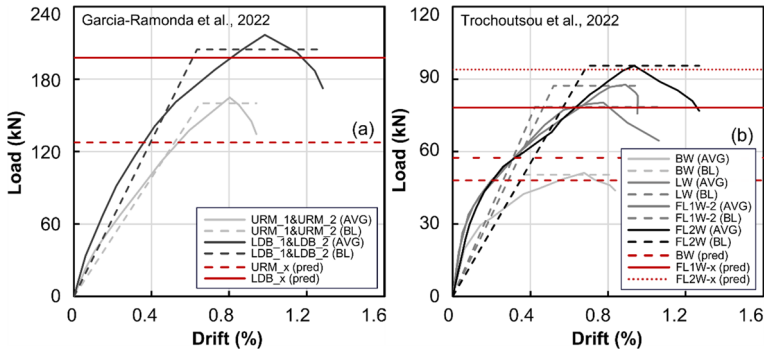


Fig. 17 Comparative capacity predictions and load-drift curves for URM and TRM-strengthened walls failing in diagonal tension: **a** non-strengthened URM_1 & URM_2 and TRM-strengthened LDB_1 & LDB_2 (Garcia-Ramonda et al. 2022); **b** non-strengthened non-rendered BW, non-strengthened and rendered LW, TRM-strengthened with 1 layer both sides FL1W and 2 layers both sides FL2W (Trochoutsou et al. 2022)

4.3.3 Comparative assessments and practical considerations

The response of the relatively large wall specimens described in Sect. 3.3 are compared in Fig. 16 to the EC8-3 (CEN 2021b) predictions. The black solid curves are the test envelopes, the continuous red curves represent the URM diagonal tension response estimates (full response for WA1-0, or capacity for WA1-2), the dashed red curve represents the TRM activation using Eq. (15), the dashed grey curves are the URM flexural load drift curves, and the dash-dot grey line is the URM flexural response estimates multiplied by $\beta = 1.15$ accounting for the confinement produced by the TRM overlay suggested in Sect. 4.2. Figure 16 indicate that the design code predicts generally well both the diagonal tension and flexural load drift-envelopes as well as the governing mechanism; i.e. the diagonal tension capacity is below the flexural capacity for WA1-0.

As shown in Fig. 17a, b the diagonal tension capacity predictions using the EC8-3 expressions, shown in dashed red lines, provide slightly conservative estimates compared with existing URM tests (i.e. Specimens URM_1 & URM_2 from Garcia-Ramonda et al. 2022; and Specimen BW from Trochoutsou et al. 2022). The load-drift curves in the figure are assessed from the average of the positive and negative envelopes, and using the bilinearisation procedure described in Sect. 3.3. The beneficial contribution of the mortar overlay, without the presence of textile meshes is shown by the comparative load-drift curves of non-rendered Specimen BW and rendered Specimen LW in Fig. 17b. The dashed-dot red line indicates the cumulative contribution of the masonry through diagonal tension (Eq. 6c) and of the render (Eq. 15c). This is below the peak capacity of the LW wall, indicating a conservative prediction of the capacity. Finally, the cumulative contribution of the masonry, render and textiles (Eq. 6a and Eq. 15) for TRM-strengthened walls failing in diagonal tension is shown in Fig. 17 as a continuous red line for walls with one textile meshes both sides (LDB_1 & LDB_2 and FL1W), and as dotted red line for walls with two textile meshes both sides. For these assessments, a reduced ultimate fibre strain $\epsilon_f = 0.006$ was considered, to account for the strain concentration and partial/local activation of the mesh at the maximum crack width, crack kinematics and crack pattern due to cyclic loading. It is shown that the predicted capacities are below peak test strength, indicating safe application of the proposed model for TRM-strengthened walls failing in diagonal tension.

Table 4 Comparative drift capacities of URM and TRM-strengthened walls in the literature

Author	ID	d × h × t (mm)	Bricks type (-)	Joint mortar (-)	Overlay mortar (-)	Textile (-)	Render sides (-)	Layers/ side (-)	N (kN)	V _{peak} (kN)	FM	Δ _y (%)	Δ _u (%)	Δ _{uTRM} / Δ _{uURM} (-)
This paper	WA1-0	1910 × 1310 × 110	Solid clay bricks	Lime	-	-	0	0	227	110	DT	0.15	0.63	-
	WA1-2	1910 × 1310 × 110	Solid clay bricks	Lime	Lime-cement	Glass	2	2	224	143	TC	0.08	1.46	2.30
Torres et al. 2021	URM	3000 × 2000 × 230	Solid clay bricks	Lime	-	-	0	0	150	139	DT	0.30	0.53	-
	DRW*	3000 × 2000 × 230	Solid clay bricks	Lime	Lime & fibres	Glass	2	1	150	340	DT	0.31	0.66	1.25
	NDRW	3000 × 2000 × 230	Solid clay bricks	Lime	Lime & fibres	Glass	2	1	150	340	DT	0.52	0.72	1.35

Table 4 (continued)

Author	ID	d × h × t (mm)	Bricks type (-)	Joint mortar (-)	Overlay mortar (-)	Textile (-)	Render sides (-)	Layers/ side (-)	N (kN)	V _{peak} (kN)	FM	Δ _y (%)	Δ _u (%)	Δ _{uTRM} / Δ _{uURM} (-)
Garcia-Ramonda et al. 2022	URM_1	1270 × 1270 × 310	Solid clay bricks	Lime	-	-	0	0	118	172	DT	0.66	0.86	-
	URM_2	1270 × 1270 × 310	Solid clay bricks	Lime	-	-	0	0	118	157	DT	0.64	1.02	-
	URM1_R*	1270 × 1270 × 310	Solid clay bricks	Lime	Lime	Basalt	2	1	118	179	DT	0.55	1.28	1.36
	URM2_R*	1270 × 1270 × 310	Solid clay bricks	Lime	Lime	Basalt	2	1	118	182	DT	0.63	1.54	1.63
	LDB_1	1270 × 1270 × 310	Solid clay bricks	Lime	Lime	Basalt	2	1	118	211	DT	0.75	1.46	1.55
	LDB_2	1270 × 1270 × 310	Solid clay bricks	Lime	Lime	Basalt	2	1	118	222	DT	0.52	1.11	1.18

Table 4 (continued)

Author	ID	d × h × t (mm)	Bricks type (-)	Joint mortar (-)	Overlay mortar (-)	Textile (-)	Render sides (-)	Layers/ side (-)	N (kN)	V _{peak} (kN)	FM	Δ _y (%)	Δ _u (%)	Δ _{uTRM} / Δ _{uURM} (-)
Meriggi et al. 2022	UM	1200 × 1200 × 250	Rubble lime-stone	Lime	-	-	0	0	180	121	DT	0.45	0.83	-
	UM-R	1200 × 1200 × 250	Rubble lime-stone	Lime	Lime	Basalt	2	1	180	153	LS	0.45	0.85	1.03**
	PM-R	1200 × 1200 × 250	Rubble lime-stone	Lime	Lime	Basalt & anchors	2	1	180	174	TC	0.50	0.81	1.04**
Trochoutsou et al. 2022	BW	1150 × 1085 × 102	Frogged clay bricks	Cement-lime	-	-	0	0	70	51	DT	0.37	0.84	-
	FL1W-2	1098 × 1110 × 102	Frogged clay bricks	Cement-lime	Lime & fibres	Flax	2	2	70	88	DT	0.52	0.95	1.14
	FL2W-1	1150 × 1120 × 102	Frogged clay bricks	Cement-lime	Lime & fibres	Flax	2	1	70	96	DT	0.69	1.27	1.52
	FL2W-2	1108 × 1075 × 102	Frogged clay bricks	Cement-Lime	Lime & fibres	Flax	2	2	70	103	DT	0.79	1.44	1.72
												Average	1.42	

FM failure mode, DT diagonal tension, TC toe crushing, LS leaf separation
 *Damaged and repaired; **drift capacity of the rig reached during tests; italics indicate URM walls

For the tests described in this paper, the URM diagonal tension capacity for WA1-2 is lower than the flexural capacity, but the latter is only 7% higher, indicating that rocking is activated immediately after the URM shear resistance is reached (Fig. 16b). The dashed-dotted grey curve indicates that the TRM enhanced the flexural capacity delaying toe crushing mode, attributed to the confinement action provided by the overlay. With regards to deformation response, the code curves align very well with the test envelopes. For WA1-2, there is a significant increase in ductility and more representative drift limits may be considered in practice, provided that the TRM is adequately bonded and anchored in the masonry wall; i.e. leaf separation and/or buckling are prevented. This is supported by the TRM-strengthened-to-URM ultimate drift capacities ($\Delta_{u,TRM}/\Delta_{u,URM}$) shown in Table 4 for the tests in this paper and in the literature. It is shown that the average $\Delta_{u,TRM}/\Delta_{u,URM} = 1.42$ which are within the ranges suggested in the revised EC8-3 (CEN,2021b). As stipulated in EC8-1-2 (CEN 2021c) and EC8-3 (CEN 2021b), the drift capacity of reinforced masonry members may be assumed as 1.5 times and 1.33 times those of URM, respectively, unless

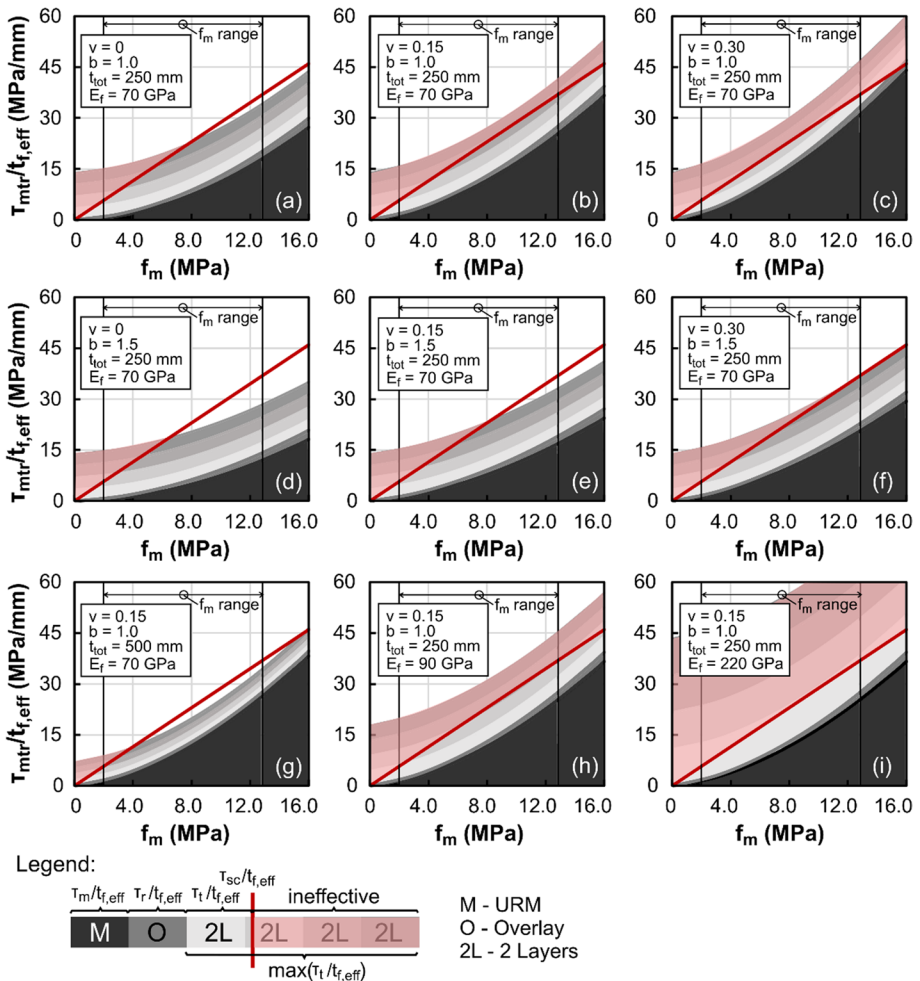


Fig. 18 Relationship between masonry compressive strength and normalised shear capacity

other values are demonstrated by tests and provided that details are compatible with those in EC6 (CEN 2005a). It is shown that for TRM-strengthened walls failing in diagonal tension, the EC8-3 approach would give more conservative ultimate drift estimates.

To illustrate the comparative influence of key material and geometric properties on the effectiveness of TRM in strengthening heritage URM walls governed by diagonal tension failure, Fig. 18 is constructed as an indicative guide. The curves depicted in Fig. 18 are obtained from Eq. (15), where the total wall thickness t_{tot} , axial load ratio ν , wall aspect ratio correction parameter b , and the type of mesh material were varied, with other parameters kept constant. For comparative purposes only, $t_{tot}=250$ and 500 mm (in which t_{tot} is the sum of masonry t and overlay t_r thicknesses) were considered. The overlay thickness $t_r=10(n_f+2)/3$ was obtained from a linear regression of the measured thickness t_r and number of layers n_f of the TRM coupons described in Sect. 2.2. Axial load ratios of $\nu=0$, 0.15 and 0.30 and aspect ratio parameters of $b=1.0$ and 1.5, were considered. These ν are typical for masonry walls in heritage structures (Guo et al. 2022a), whilst the two b values are the lower and upper bounds stipulated in EC8-3 (CEN 2021b). Finally, meshes with a reduced ultimate fibre strain $\epsilon_f=0.006$ and elastic modulus of $E_f=70$, 90 and 220 GPa, corresponding to typical ranges for glass, basalt and carbon materials, were accounted for.

The abscissa of Fig. 18 shows compressive strength f_m ranges of clay brick lime mortar masonry, representative of heritage structures, which can be estimated from the material properties of the bricks and mortars (Bompa and Elghazouli 2021). The y-axis shows the normalised cumulative shear strength ($\tau_{mr}/t_{f,eff}$) in which $\tau_{mr}=V_{mr}/(t \times d)$ and $t_{f,eff}=\Sigma A_f/h$ as defined in Sect. 4.2.3 and Fig. 13. As shown in the legend of the figure, the contributions of the URM, overlay and each two consecutive mesh layers (one on each side of the wall) are identified with 'M', 'O' and '2L', respectively, and illustrated in a different colour. To assess the contribution of the URM, $f_r=0.0163f_m^{1.88}$ was obtained from a regression analysis from the tests in Sect. 3.2 and values stipulated in EC8-3 (CEN 2021b). The code gives a single value $f_r=0.114 \pm 0.21$ MPa for solid brick masonry and lime mortar having an $f_m=3.4 \pm 0.26$ MPa, thus giving unreliable estimates outside this value. The contribution of the overlay and of the TRM was assessed using Eq. (15) and associated assumptions. Finally, the $\tau_{mr}/t_{f,eff}$ at which strut crushing (SC) may govern is shown by a continuous red line (Eq. 15d) and in light red shade. Note that flexural-response modes can also govern the limit condition, capping the $\tau_{mr}/t_{f,eff}$ both for URM and TRM-strengthened walls. These response modes need to be verified independently for each configuration as they are boundary conditions-dependent (Eq. 7).

It is generally shown from Fig. 18 that for relatively low strength masonry ($f_m \approx 2$ MPa), SC governs and a maximum of 2L will be activated achieving ϵ_f around 0.006. With gradual increase in f_m , a higher number of layers are activated, and SC would gradually govern in proportion to the increase in ν , as evidenced by the trends in Fig. 18a–c. Similar trends appear in Fig. 18d–f, yet a lower URM contribution is observed due to the comparatively higher aspect ratio correction parameter ($b=1.5$) considered. A comparatively thicker wall ($t_{tot}=500$ mm) would lead to a high contribution from the TRM for low f_m and a low contribution from TRM for high f_m values (Fig. 18g). For example, for $f_m \approx 2$ MPa each 2L of TRM would double the $\tau_{mr}/t_{f,eff}$ value but is limited by SC, whilst for $f_m \approx 8$ MPa, the enhancement will only be around 25%. Using a mesh with higher E_f would give higher contribution from the TRM for each 2L of mesh, which may be more practical as n_f is reduced, leading to less workmanship and thinner TRMs for the same required $\tau_{mr}/t_{f,eff}$ capacity. Such comparative illustrations may be useful in practice to evaluate the efficacy of TRM strengthening and support decisions on selective intervention techniques.

5 Conclusions

This paper examined the experimental response of unreinforced masonry (URM) elements incorporating fired clay brick and hydraulic lime mortar, representative of many heritage structures, strengthened with textile reinforced mortar (TRM). Tests on URM and TRM components, URM and TRM-strengthened diagonal compression elements, and wall specimens subjected to gravity loading and lateral cyclic deformations, were carried out. The results enabled a detailed assessment of the influence of TRM overlays on the stiffness, strength, energy dissipation and deformation capacity, as well as evaluation and improvement of analytical models for determining the key inelastic response parameters. The main remarks are outlined below.

- Compression tests indicated a linear relationship between the compressive strength of masonry and the mortar joint strength given a constant brick unit strength. Elastic modulus-to-compressive strength ratios between 175 and 260 were also obtained, which are lower than those of cement mortars.
- The TRM stress–strain curves showed a distinctive bi-linear response with ultimate strength and fracture strain depending on the mortar thickness and the number of textile layers. An increase from 1 to 2 layers led to an enhancement in strength and fracture strain by 82.6% and 38.2%, respectively, whilst an increase from 2 to 4 layers added a further 32.5% and 7.8%, respectively. Single-lap bond tests showed that substrate-TRM debonding does not govern the response.
- Diagonal compression tests showed that the enhancements in stiffness and strength are not directly proportional to the number of layers, depending on the render thickness, overlay and substrate strengths. A single layer of mesh on both surfaces of the panel led to stiffness, strength and ultimate shear strain enhancement of 49%, 102% and 300% respectively. The use of two layers increased the same parameters on average by 94%, 230% and 556%, whilst for four layers the enhancements were by 132%, 536% and 532%, respectively.
- Strut crushing can govern the response of TRM-strengthened panels with relatively low URM compressive strength due to the confinement provided by adequately tied TRM overlays. Strut stress-to-masonry compressive strength ratios of 1.17, 1.23 and 1.63 corresponding to one, two and four mesh layers, respectively, were estimated for the tests described in this paper, which are comparable to expected biaxial strengths in brittle materials.
- For URM walls failing in diagonal tension under combined lateral cyclic and gravity loading, the addition of TRM overlays restricted diagonal crack development, shifting the response to rocking. The addition of TRM overlays enhanced the stiffness by 167% and increased the strength by 30.6% compared to the non-rendered counterpart.
- A shift from URM diagonal tension to toe crushing in the large TRM-strengthened wall produced an increase in ultimate drift capacity by 132% as well as a 108% higher cumulative energy at ultimate. For the URM and TRM-strengthened walls failing in flexure, although the drift capacities were similar, the latter had 29.3% higher energy dissipation. The first-to-second cycle strength degradation was higher than for the second-to-third cycle in all cases.
- Analytical assessments indicated that considering a cumulative contribution of the URM and TRM overlay, with their specific geometries and measured material properties, predicts well the stiffness of the strengthened diagonal panels. Provided that

debonding or leaf separation do not occur, a cumulative contribution of the masonry, mortar, and textile strengths considering the fracture strain of the textile mesh, provides an improved in-plane strength estimate compared to current code predictions.

- Code expressions were shown to predict generally well the governing mechanism and capacity for URM walls under lateral loading. However, for the TRM contribution, a reduced fibre strain of 0.6% was considered in the current assessments to account for specific crack kinematics and crack patterns due to cyclic loading. This reduced strain is 50% higher than typically imposed by codes and provided a safe capacity prediction for a range of tests extracted from the literature.
- The average TRM-strengthened to URM wall ultimate drift capacity ratios based on tests from the literature was 1.42 which is within the ranges stipulated in seismic design codes for reinforced masonry, suggesting that the current provisions are suitable for estimating the ultimate drift capacity of TRM-strengthened masonry walls.
- Based on the proposed analytical relationships, the comparative influence of key material and geometric properties on the effectiveness of TRM in strengthening heritage URM walls governed by diagonal tension failure was illustrated through representative curves. Such curves may be useful in practice as an indicative guide for supporting decisions on selective intervention techniques.

Acknowledgements The study was carried out within the project “Interdisciplinary approach for the management and conservation of UNESCO World Heritage Site of Historic Cairo - Application to Al-Ashraf Street” supported by the Newton-Mosharafa funding programme, a joint fund by the Science, Technology and Innovation Funding Authority (STIFA) of Egypt, Grant No. AHRC30799 and the Arts and Humanities Research Council (AHRC) of the UK, Grant No. AH/R00787X/1. The authors would also like to acknowledge the support provided by the technical staff of the Structures Laboratories at Imperial College London, particularly Mr. P. Crude and Mr. L. Clark.

Author contributions All authors contributed to the study conception and design. Detailed methodology, investigation and original drafting were carried out by A.Y. Elghazouli and D.V. Bompa. All authors commented on previous versions of the manuscript and approved the final manuscript.

Funding The study was supported by the Arts and Humanities Research Council of the UK Research and Innovation agency, within the project “Interdisciplinary approach for the management and conservation of UNESCO World Heritage Site of Historic Cairo - Application to Al-Ashraf Street”, Grant No. AH/R00787X/1, and the Science, Technology and Innovation Funding Authority (STIFA) of Egypt, Grant No. AHRC30799.

Data availability Selected data for this study is accessible upon written request.

Declarations

Conflict of interest There are no conflicts of interest for this paper.

Informed consent and ethical approval No informed consents or ethical approvals are required for the research presented in this paper.

Open Access This article is licensed under a Creative Commons Attribution 4.0 International License, which permits use, sharing, adaptation, distribution and reproduction in any medium or format, as long as you give appropriate credit to the original author(s) and the source, provide a link to the Creative Commons licence, and indicate if changes were made. The images or other third party material in this article are included in the article’s Creative Commons licence, unless indicated otherwise in a credit line to the material. If material is not included in the article’s Creative Commons licence and your intended use is not permitted by statutory regulation or exceeds the permitted use, you will need to obtain permission directly from the copyright holder. To view a copy of this licence, visit <http://creativecommons.org/licenses/by/4.0/>.

References

- ACI (American Concrete Institute) (2013) ACI 549.4R6R-13. Guide to design and construction of externally bonded fabric-reinforced cementitious matrix (FRCM) and steel-reinforced grout (SRG) systems for repair and strengthening masonry structures. American Concrete Institute, Farmington Hills, MI
- ACI (American Concrete Institute) (2013) ACI 549.6R-20. Guide to design and construction of externally bonded fabric-reinforced cementitious matrix (FRCM) and steel-reinforced grout (SRG) systems for repair and strengthening masonry structures. American Concrete Institute, Farmington Hills, MI
- Almeida JAPP, Pereira EB, Barros JAO (2015) Assessment of overlay masonry strengthening system under in-plane monotonic and cyclic loading using the diagonal tensile test. *Constr Build Mater* 94:851–865. <https://doi.org/10.1016/j.conbuildmat.2015.07.040>
- ASCE (American Society of Civil Engineers) (2017) ASCE/SEI 41-17 seismic evaluation and retrofit of existing buildings. ASCE (American Society of Civil Engineers), Reston, VA
- ASTM E519-07 (2017) Standard test method for diagonal tension (shear) in masonry assemblages. ASTM International
- Benedetti A, Steli E (2008) Analytical models for shear–displacement curves of unreinforced and FRP reinforced masonry panels. *Constr Build Mater* 22(3):175–185. <https://doi.org/10.1016/j.conbuildmat.2006.09.005>
- Bertolesi E, Carozzi FG, Milani G, Poggi C (2014) Numerical modeling of Fabric Reinforced Cementitious Matrix composites (FRCM) in tension. *Constr Build Mater* 70:531–548. <https://doi.org/10.1016/j.conbuildmat.2014.08.006>
- Bertolesi E, Buitrago M, Giordano E, Calderon PA, Moragues JJ, Clementi F, Adam JM (2020) Effectiveness of textile reinforced mortar (TRM) materials in preventing seismic-induced damage in a U-shaped masonry structure submitted to pseudo-dynamic excitations. *Constr Build Mater* 248:118532. <https://doi.org/10.1016/j.conbuildmat.2020.118532>
- Bompa DV, Elghazouli AY (2020) Experimental and numerical assessment of the shear behaviour of lime mortar clay brick masonry triplets. *Constr Build Mater* 262:120571. <https://doi.org/10.1016/j.conbuildmat.2020.120571>
- Bompa DV, Elghazouli AY (2021) Mechanical properties of hydraulic lime mortars and fired clay bricks subjected to dry-wet cycles. *Constr Build Mater* 303:124458. <https://doi.org/10.1016/j.conbuildmat.2021.124458>
- Bompa DV, Elghazouli AY (2022) Shear-compression failure envelopes for clay brick lime mortar masonry under wet and dry conditions. In: Vayas I, Mazzolani FM (eds) Protection of historical constructions (PROHITECH 2021). Lecture notes in civil engineering, vol 209. Springer, Cham. https://doi.org/10.1007/978-3-030-90788-4_17
- Bosiljkov VZ, Totoev YZ, Nichols JM (2005) Shear modulus and stiffness of brickwork masonry: an experimental perspective. *Struct Eng Mech* 20(1):21–44
- Breedon Cement Limited (2019) High Strength 52.5N Cement. https://www.breedongroup.com/images/uploads/products/Portland_Plus_Cement_DS.pdf. Accessed 25 Feb 2019
- Calderini C, Cattari S, Lagomarsino S (2010) The use of the diagonal compression test to identify the shear mechanical parameters of masonry. *Constr Build Mater* 24(5):677–685. <https://doi.org/10.1016/j.conbuildmat.2009.11.001>
- Calvi GM, Kingsley GR, Magenes G (1996) Testing of masonry structures for seismic assessment. *Earthq Spectra* 12(1):145–162. <https://doi.org/10.1193/1.1585872>
- CEN (European Committee for Standardization) (1999a) EN 1015-2:1999 methods of test for mortar for masonry—Part 2: bulk sampling of mortars and preparation of test mortars. European Committee for Standardization, Brussels
- CEN (European Committee for Standardization) (1999b) EN 1015-3:1999 methods of test for mortar for masonry—part 3: determination of consistence of fresh mortar (by flow table). European Committee for Standardisation, Brussels
- CEN (European Committee for Standardization) (1999d) EN 1052-1:1999 methods of test for masonry. Determination of compressive strength. European Committee for Standardisation, Brussels
- CEN (European Committee for Standardization) (2004) EN 1998-1: 2004: Eurocode 8: Design of structures for earthquake resistance. Part 1: general rules, seismic actions and rules for buildings. European Committee for Standardisation, Brussels.
- CEN (European Committee for Standardization) (2005a) EN 1996-1-1: 2005 Eurocode 6: design of masonry structures—general rules for reinforced and unreinforced masonry structures. European Committee for Standardisation, Brussels


- CEN (European Committee for Standardization) (2005b) EN 1998-3: 2005: Eurocode 8. Design of structures for earthquake resistance. Assessment and Retrofitting of Buildings. European Committee for Standardisation, Brussels
- CEN (European Committee for Standardization) (2013) EN ISO 13934-1:2013 Textiles. Tensile properties of fabrics. Determination of maximum force and elongation at maximum force using the strip method. European Committee for Standardisation, Brussels
- CEN (European Committee for Standardization) (2021a) EN 459-2. Building lime: test methods. European Committee for Standardisation, Brussels
- CEN (European Committee for Standardization) (2021b) Eurocode 8: design of structures for earthquake resistance—Part 3: assessment and retrofitting of buildings and bridges. European Committee for Standardisation, Brussels
- CEN (European Committee for Standardization) (2021c) Eurocode 8: design of structures for earthquake resistance—Part 1-2: rules for new buildings. European Committee for Standardisation, Brussels
- Ceresit (2022) CT325 glass-fibre mesh reinforcing mesh. Online. <https://www.ceresit.com/en/products/facade-solutions/facade-accessoires/system-accessories/ceresit-ct-325.html>. Accessed 18 Sept 2022
- CNR (Advisory Committee on Technical Recommendations for Construction) (2018) CNR-DT 215/2018 guide for the design and construction of fibre reinforced inorganic matrix systems for strengthening existing structures. Rome—CNR 06.02.2019; version of June 30, 2020
- Corinaldesi V (2012) Environmentally-friendly bedding mortars for repair of historical buildings. *Constr Build Mater* 35:778–784. <https://doi.org/10.1016/j.conbuildmat.2012.04.131>
- Costigan A, Pavia S, Kinnane O (2015) An experimental evaluation of prediction models for the mechanical behavior of unreinforced, lime-mortar masonry under compression. *J Build Eng* 4:283–294. <https://doi.org/10.1016/j.jobe.2015.10.001>
- D'Anna J, Amato G, Chen JF, Minafò G, La Mendola L (2021) Experimental application of digital image correlation for the tensile characterization of basalt FRCM composites. *Constr Build Mater* 271:121770. <https://doi.org/10.1016/j.conbuildmat.2020.121770>
- D'Ayala D, Speranza E (2003) Definition of collapse mechanisms and seismic vulnerability of historic masonry buildings. *Earthq Spectra* 19(3):479–509. <https://doi.org/10.1193/1.1599896>
- Donnini J, Maracchini G, Lenci S, Corinaldesi V, Quagliarini E (2021) TRM reinforced tuff and fired clay brick masonry: Experimental and analytical investigation on their in-plane and out-of-plane behavior. *Constr Build Mater* 272:21643. <https://doi.org/10.1016/j.conbuildmat.2020.121643>
- Egernsund Tegl (2019) Chelmer Red Imperial. <https://www.egernsund-tegl.com/products/bricks/270-2.2.07-chelmer-red-imperial>. Accessed 10 Nov 2019
- Elghazouli A, Butler A, Mourad S, Cheeseman C, Elyamani A, (2018) Interdisciplinary approach for the management and conservation of UNESCO World Heritage Site of Historic Cairo. Application to Al-Ashraf Street. UK Research and Innovation. Accessed 10 Jan 2023. <https://gtr.ukri.org/projects?ref=AH%2FR00787X%2F1>
- Elghazouli AY, Bompá DV, Mourad SA, Elyamani A (2021) In-plane lateral cyclic behaviour of lime-mortar and clay-brick masonry walls in dry and wet conditions. *Bull Earthq Eng* 19(13):5525–5563. <https://doi.org/10.1007/s10518-021-01170-5>
- Elghazouli AY, Bompá DV, Mourad SA, Elyamani A (2022a) Structural behaviour of clay brick lime mortar masonry walls under lateral cyclic loading in dry and wet conditions. In: Vayas I, Mazzolani FM (eds) Protection of historical constructions (PROHITECH 2021). Lecture notes in civil engineering, vol 209. Springer, Cham. https://doi.org/10.1007/978-3-030-90788-4_16
- Elghazouli AY, Bompá DV, Mourad SA, Elyamani A (2022b) Seismic performance of heritage clay brick and lime mortar masonry structures. In: Vacareanu R, Ionescu C (eds) Progresses in European earthquake engineering and seismology (ECEES 2022). Springer proceedings in earth and environmental sciences. Springer, Cham. https://doi.org/10.1007/978-3-031-15104-0_14
- Faella C, Martinelli E, Nigro E, Paciello S (2010) Shear capacity of masonry walls externally strengthened by a cement-based composite material: an experimental campaign. *Constr Build Mater* 24:84–93. <https://doi.org/10.1016/j.conbuildmat.2009.08.019>
- Ferrara G, Caggegi C, Martinelli E, Gabor A (2020) Shear capacity of masonry walls externally strengthened using Flax–TRM composite systems: experimental tests and comparative assessment. *Constr Build Mater* 261:120490. <https://doi.org/10.1016/j.conbuildmat.2020.120490>
- Fortunato G, Funari MF, Lonetti P (2017) Survey and seismic vulnerability assessment of the Baptistery of San Giovanni in Tumba (Italy). *J Cult Herit* 26:64–78. <https://doi.org/10.1016/j.culher.2017.01.010>
- Garcia-Ramonda L, Pelà L, Roca P, Camata G (2022) Cyclic shear-compression testing of brick masonry walls repaired and retrofitted with basalt textile reinforced mortar. *Compos Struct* 283:115068. <https://doi.org/10.1016/j.compstruct.2021.115068>

- Gattesco N, Amadio C, Bedon C (2015) Experimental and numerical study on the shear behavior of stone masonry walls strengthened with GFRP reinforced mortar coating and steel-cord reinforced repointing. *Eng Struct* 90:143–157. <https://doi.org/10.1016/j.engstruct.2015.02.024>
- Guo YT, Bompa DV, Elghazouli AY (2022a) Nonlinear numerical assessments for the in-plane response of historic masonry walls. *Eng Struct* 268:114734. <https://doi.org/10.1016/j.engstruct.2022.114734>
- Guo YT, Bompa DV, Elghazouli AY (2022b) Numerical modelling of the cyclic behaviour of clay brick and lime mortar masonry elements. In: Proceedings of the third European conference on earthquake engineering and seismology—3ECEES, September 5–September 9, 2022. Conspress, Bucharest, pp 1054–1061
- Haach VG, Vasconcelos G, Lourenço PB (2010) Experimental analysis of reinforced concrete block masonry walls subjected to in-plane cyclic loading. *J Struct Eng* 136(4):452–462. [https://doi.org/10.1061/\(ASCE\)ST.1943-541X.0000125](https://doi.org/10.1061/(ASCE)ST.1943-541X.0000125)
- Hendry AW (1997) Shear strength criteria and related tests for brick masonry. *Adv Struct Eng* 1(2):135–141
- Hračov S, Pospíšil S, Garofano A, Urushadze S (2016) In-plane cyclic behaviour of unfired clay and earth brick walls in both unstrengthened and strengthened conditions. *Mater Struct* 49(8):3293–3308. <https://doi.org/10.1617/s11527-015-0720-5>
- Ismail N, Ingham JM (2014) Polymer textiles as a retrofit material for masonry walls. *Proc Inst Civ Eng Struct Build* 167(1):15–25. <https://doi.org/10.1680/stbu.11.00084>
- Ivorra S, Torres B, Baeza FJ, Bru D (2021) In-plane shear cyclic behavior of windowed masonry walls reinforced with textile reinforced mortars. *Eng Struct* 226:111343. <https://doi.org/10.1016/j.engstruct.2020.111343>
- Kadam SB, Singh Y, Li B (2014) Strengthening of unreinforced masonry using welded wire mesh and micro-concrete—behaviour under in-plane action. *Constr Build Mater* 54:247–257. <https://doi.org/10.1016/j.conbuildmat.2013.12.033>
- Koutas LN, Bournas DA (2020) Confinement of masonry columns with textile-reinforced mortar jackets. *Constr Build Mater* 258:120343. <https://doi.org/10.1016/j.conbuildmat.2020.120343>
- Koutas L, Bousias SN, Triantafillou TC (2014) Seismic strengthening of masonry-infilled RC frames with TRM: experimental study. *J Compos Constr* 19(2):04014048. [https://doi.org/10.1061/\(ASCE\)CC.1943-5614.0000507](https://doi.org/10.1061/(ASCE)CC.1943-5614.0000507)
- Kupfer H, Hilsdorf HK, Rusch H (1969) Behavior of concrete under biaxial stresses. *ACI J Proc* 66(8):656–666
- LaVision (2022) DaVis digital image correlation software <http://www.lavision.de/en/products/davis-software/index.php>. Accessed 10 Nov 2022
- Li T, Galati N, Tumialan JG, Nanni A (2005) Analysis of unreinforced masonry concrete walls strengthened with glass fiber-reinforced polymer bars. *ACI Struct J* 102(4):569
- Magenes G, Galasco A, Penna A, Da Paré M (2010) In-plane cyclic shear tests of undressed double leaf stone masonry panels. In: Proceedings of the 14th European conference on earthquake engineering, Ohrid
- Marcari G, Basili M, Vestroni F (2017) Experimental investigation of tuff masonry panels reinforced with surface bonded basalt textile-reinforced mortar. *Compos B Eng* 108:131–142. <https://doi.org/10.1016/j.compositesb.2016.09.094>
- Meriggi P, Caggegi C, Gabor A, de Felice G (2022) Shear-compression tests on stone masonry walls strengthened with basalt textile reinforced mortar (TRM). *Constr Build Mater* 316:125804. <https://doi.org/10.1016/j.conbuildmat.2021.125804>
- Messali F, Metelli G, Plizzari G (2017) Experimental results on the retrofitting of hollow brick masonry walls with reinforced high-performance mortar coatings. *Constr Build Mater* 141:619–630. <https://doi.org/10.1016/j.conbuildmat.2017.03.112>
- Moon FL (2004) Seismic strengthening of low-rise unreinforced masonry structures with flexible diaphragms, Ph.D. thesis, Georgia Institute of Technology, Atlanta
- Papanicolaou C, Triantafillou T, Lekka M (2011) Externally bonded grids as strengthening and seismic retrofitting materials of masonry panels. *Constr Build Mater* 25(2):504–514. <https://doi.org/10.1016/j.conbuildmat.2010.07.018>
- Parisi F, Iovinella I, Balsamo A, Augenti N, Prota A (2013) In-plane behavior of tuff masonry strengthened with inorganic matrix–grid composites. *Compos B* 45(1):1657–1666. <https://doi.org/10.1016/j.compositesb.2012.09.068>
- Petry S, Beyer K (2015) Cyclic test data of six unreinforced masonry walls with different boundary conditions. *Earthq Spectra* 31(4):2459–2484. <https://doi.org/10.1193/101513EQS269>
- Prota A, Marcari G, Fabbrocino G, Manfredi G, Aldea C (2006) Experimental in-plane behavior of tuff masonry strengthened with cementitious matrix–grid composites. *J Compos Constr* 10(3):223–233. [https://doi.org/10.1061/\(ASCE\)1090-0268\(2006\)10:3\(223\)](https://doi.org/10.1061/(ASCE)1090-0268(2006)10:3(223))

- Righetti L, Edmondson V, Corradi M, Borri A (2016) Fiberglass grids as sustainable reinforcement of historic masonry. *Materials* 9(7):603. <https://doi.org/10.3390/ma9070603>
- Salmanpour AH, Mojsilovic N, Schwartz J (2013) Deformation capacity of unreinforced masonry walls subjected to in-plane loading: a state-of-the-art review. *Int J Adv Struct Eng* 5(1):22. <https://doi.org/10.1186/2008-6695-5-22>
- Secil Argamassas (2019) Natural hydraulic lime (NHL)—the binder. https://www.secilargamassas.pt/uploads/documentos/Ficha_Tecnica_NHL_5.pdf. Accessed 10 Nov 2019
- Shermi C, Dubey RN (2017) Study on out-of-plane behaviour of unreinforced masonry strengthened with welded wire mesh and mortar. *Constr Build Mater* 143:104–120. <https://doi.org/10.1016/j.conbuildmat.2017.03.002>
- Szabó S, Funari MF, Lourenço PB (2023) Masonry patterns' influence on the damage assessment of URM walls: current and future trends. *Dev Built Environ*. <https://doi.org/10.1016/j.dibe.2023.100119>
- Thomoglou AK, Rousakis TC, Achillopoulou DV, Karabinis AI (2020) Ultimate shear strength prediction model for unreinforced masonry retrofitted externally with textile reinforced mortar. *Earthq Struct* 19(6):411–425. <https://doi.org/10.12989/eas.2020.19.6.411>
- Tomazevic M (1999) Earthquake-resistant design of masonry buildings. Imperial College Press, London
- Torres B, Ivorra S, Baeza FJ, Estevan L, Varona B (2021) Textile reinforced mortars (TRM) for repairing and retrofitting masonry walls subjected to in-plane cyclic loads. An experimental approach. *Eng Struct* 231:111742
- Triantafyllou T (ed) (2016) Textile fibre composites in civil engineering. Woodhead Publishing
- Trochoutsou N, Di Benedetti M, Pilakoutas K, Guadagnini M (2022) In-plane cyclic performance of masonry walls retrofitted with flax textile-reinforced mortar overlays. *J Compos Constr* 26(5):04022049. [https://doi.org/10.1061/\(ASCE\)CC.1943-5614.0001238](https://doi.org/10.1061/(ASCE)CC.1943-5614.0001238)
- Türkmen ÖS, De Vries BT, Wijte SNM, Vermeltoort AT (2020) In-plane behaviour of clay brick masonry wall with retrofitted with single-sided fabric-reinforced cementitious matrix and deep mounted carbon fibre strips. *Bull Earthq Eng* 18(2):725–765. <https://doi.org/10.1007/s10518-019-00596-2>
- Umair S, Numada M, Amin M, Meguro K (2015) Fiber reinforced polymer and polypropylene composite retrofitting technique for masonry structures. *Polymers* 7(5):963–984. <https://doi.org/10.3390/polym7050963>
- Wang X, Lam CC, Iu VP (2019) Comparison of different types of TRM composites for strengthening masonry panels. *Constr Build Mater* 219:184–194. <https://doi.org/10.1016/j.conbuildmat.2019.05.179>
- Zampieri P, Simoncello N, Gonzalez Libreros J, Pellegrino C (2020) Bond behavior of steel fiber-reinforced mortar (SFRM) applied onto masonry substrate. *Arch Civ Mech Eng* 20(3):1–20. <https://doi.org/10.1007/s43452-020-00090-6>

Publisher's Note Springer Nature remains neutral with regard to jurisdictional claims in published maps and institutional affiliations.

Authors and Affiliations

A. Y. Elghazouli^{1,2}  · D. V. Bompa^{1,3} · S. A. Mourad⁴ · A. Elyamani⁵

✉ A. Y. Elghazouli
a.elghazouli@imperial.ac.uk

D. V. Bompa
d.bompa@surrey.ac.uk

S. A. Mourad
smourad@eng.cu.edu.eg

A. Elyamani
a_elyamani@cu.edu.eg

¹ Department of Civil and Environmental Engineering, Imperial College London, London, UK

² Department of Civil and Environmental Engineering, Hong Kong Polytechnic University, Kowloon, Hong Kong

³ School of Sustainability, Civil and Environmental Engineering, University of Surrey, Guildford, UK

⁴ Department of Structural Engineering, Cairo University, Giza, Egypt

⁵ Department of Archaeological Conservation, Cairo University, Giza, Egypt